Supplementary information

Table S1: Detailed configuration settings used for the WRF simulation for all cities

Category	Namelist variable	Value used	Selected option / scheme	Meaning in this study
Model core	–	WRF-ARW v4.3	Advanced Research WRF	Dynamical core used for all simulations
Simulation period	run_hours	720	30-day run	Each simulation covered 720 h; first 24 h excluded as spin-up
Initial/boundary forcing	interval_seconds	21600	NCEP FNL, 6-hourly	Initial and lateral boundary conditions updated every 6 h
Output frequency	history_interval	60, 60, 60	Hourly output	Meteorological fields are archived every hour
Frames per output file	frames_per_outfile	24, 24, 24	Daily file segmentation	24 hourly records per output file
Restart	restart	.false.	Restart disabled	Simulations run continuously
Nesting	max_dom	3	Three nested domains	Active domains: d01, d02, d03
Feedback	feedback	1	Two-way nesting	Information is passed from child to parent domains as well as from parent to child
Horizontal resolution	dx, dy	36000, 12000, 4000 m	36, 12, 4 km	Horizontal grid spacing of d01, d02, d03
Nest ratio	parent_grid_ratio	1, 3, 3	1:3 nesting ratio	Refinement from d01→d02 and d02→d03

Time-step ratio	parent_time_step_ratio	1, 3, 3	Parent-child time-step ratio	Nested time stepping consistent with grid refinement
Domain size	e_we, e_sn	65×79; 73×79; 97×103	Grid dimensions	Horizontal extent of each active domain
Vertical coordinate	e_vert	41	41 eta levels	Vertical discretization used in all active domains
Model top	p_top_requested	5000 Pa	50 hPa	Upper boundary of the model atmosphere
Adaptive time step	use_adaptive_time_step	.true.	Adaptive stepping enabled	Model time step adjusted automatically for stability
Base time step	time_step	60 s	Initial/base time step	Nominal parent-domain time step
Microphysics	mp_physics	6, 6, 6	WSM6	WRF Single-Moment 6-class microphysics scheme
Longwave radiation	ra_lw_physics	4, 4, 4	RRTMG	Rapid Radiative Transfer Model for longwave radiation
Shortwave radiation	ra_sw_physics	4, 4, 4	RRTMG	Rapid Radiative Transfer Model for shortwave radiation
Radiation time step	radt	5, 5, 5	5 min	Radiation tendencies updated every 5 min in active domains
Surface-layer physics	sf_sfclay_physics	1, 1, 1	Revised MM5 similarity	Surface exchange of momentum and heat
Land-surface model	sf_surface_physics	2, 2, 2	Noah LSM	Land-surface energy and

				moisture processes
Urban physics	sf_urban_physics	0, 0, 0	No explicit urban canopy model	Urban areas represented through bulk urban land-use treatment
PBL scheme	bl_pbl_physics	1, 1, 1	YSU	Yonsei University planetary boundary-layer scheme
Cumulus parameterisation	cu_physics	1, 0, 0	Kain–Fritsch in d01 only; off in d02–d03	Deep convection parameterised only in the outermost domain; turned off in 12 and 4 km domains. In WRF, cu_physics = 1 is Kain–Fritsch and cu_physics = 0 means no cumulus scheme. (GitHub)
Cumulus-radiation feedback	cu_rad_feedback	.true., .false., .false.	Enabled only in d01	Radiation interacts with parameterised cumulus only in the outermost domain
Soil layers	num_soil_layers	4	Four-layer soil column	Noah LSM soil discretization
Land-use categories	num_land_cat	21	21-category land-use dataset	Land-use classification used by WRF
SST update	sst_update	1	SST updating enabled	Sea-surface temperature fields updated during the run
Topographic smoothing	smooth_cg_topo	.true.	Enabled	Coarse-grid topography smoothing applied
Dynamical core mode	non_hydrostatic	.true., .true., .true.	Non-hydrostatic	Fully compressible non-hydrostatic ARW formulation

Vertical coordinate option	hybrid_opt	2	Hybrid vertical coordinate	Terrain-following hybrid coordinate
Diffusion option	diff_opt	1, 1, 1	Simple diffusion option	Horizontal/vertical diffusion framework selected
Turbulent mixing option	km_opt	4, 4, 4	Turbulent mixing formulation	Diffusion coefficient treatment consistent across domains
Upper-level damping	damp_opt	3	Rayleigh damping option	Reduces reflection near model top
Damping depth	zdamp	5000 m	Top damping layer	Damping applied in upper 5 km of the model atmosphere
Specified boundaries	specified	.true., .false., .false.	Specified boundary in d01 only	d01 receives external lateral boundary conditions
Nested boundaries	nested	.false., .true., .true.	Nested boundaries for d02–d03	Inner domains receive boundary conditions from their parent domains
I/O format	io_form_history, io_form_input, io_form_boundary, io_form_restart	2	NetCDF	Standard WRF NetCDF input/output format

S1. Evaluation of WRF simulations against ERA5

To assess whether the WRF simulations reproduced the large-scale meteorological state with sufficient realism, we evaluated the simulated near-surface meteorology against ERA5 reanalysis for May 2024 and October 2024. The primary evaluation was performed at hourly resolution. A complementary day/night composite comparison was also carried out to maintain consistency with the day and night-based framework used in the main analysis. Both validation figures are provided in the Supplementary Information (Figure S1 and S2)

ERA5 data were extracted from the nearest grid point to each prescribed city-centre coordinate using hourly reanalysis fields at 0.25° × 0.25° resolution. For WRF, city-representative values were defined as the spatial mean over the inner four radial rings (0-20 km from the city centre), so that the sampled WRF area remained broadly comparable to the effective spatial scale of a single ERA5 grid cell. Exact one-to-one agreement is not expected because the two datasets differ in spatial resolution, surface representation, and sampling definition. The purpose of this evaluation was therefore not exact value matching, but rather to assess whether the downscaled WRF fields reproduce the major inter-city meteorological contrasts and temporal variability represented in ERA5. For the day-night comparison, the matched hourly ERA5 and WRF datasets were converted to local time using city-specific UTC offsets, classified into daytime and nighttime periods using the same local-time framework as in the main analysis, and then aggregated to monthly daytime and nighttime means for each city and variable. Model performance was quantified using scatter plots and standard statistical metrics, including the Pearson correlation coefficient (r), root mean square error (RMSE), and mean bias (WRF-ERA5).

The hourly WRF-ERA5 comparison indicates that T is reproduced most consistently in both months (Figure S1), with very high correlations in May and October ($r = 0.96$ in both months), moderate RMSE values (2.76 and 2.46 °C, respectively), and a positive mean bias of about 1.3 °C. This indicates that WRF tends to simulate warmer urban-core temperatures than ERA5, which is physically plausible because WRF values represent an urban-core average, whereas ERA5 samples may not be able to isolate urban effects to the same extent. For PBLH, the hourly agreement is weaker than for temperature but remains positive and physically meaningful, with correlations of 0.83 in May and 0.80 in October. WRF generally simulates deeper boundary layers than ERA5, as reflected in the positive mean bias (140.7 m in May and 86.9 m in October), while the broader spread is consistent with the stronger sensitivity of boundary-layer height to local turbulence, surface forcing, and atmospheric stability. For WS10, the hourly comparison shows the weakest but still useful agreement, with correlations of 0.62 in May and 0.70 in October, RMSE values of 1.57 and 1.34 m s^{-1}, and a modest positive bias, indicating that WRF tends to simulate slightly stronger near-surface winds than ERA5. The complementary day/night composite comparison shows a similar ranking of model performance (Figure S2), with the strongest agreement for T_{2m} and weaker but still useful correspondence for PBLH and WS10. Taken together, the hourly and composite-based evaluations indicate that the downscaled WRF simulations reproduce the main temporal and inter-city meteorological variability with sufficient consistency for the present relative urban-core versus outer-ring analysis.

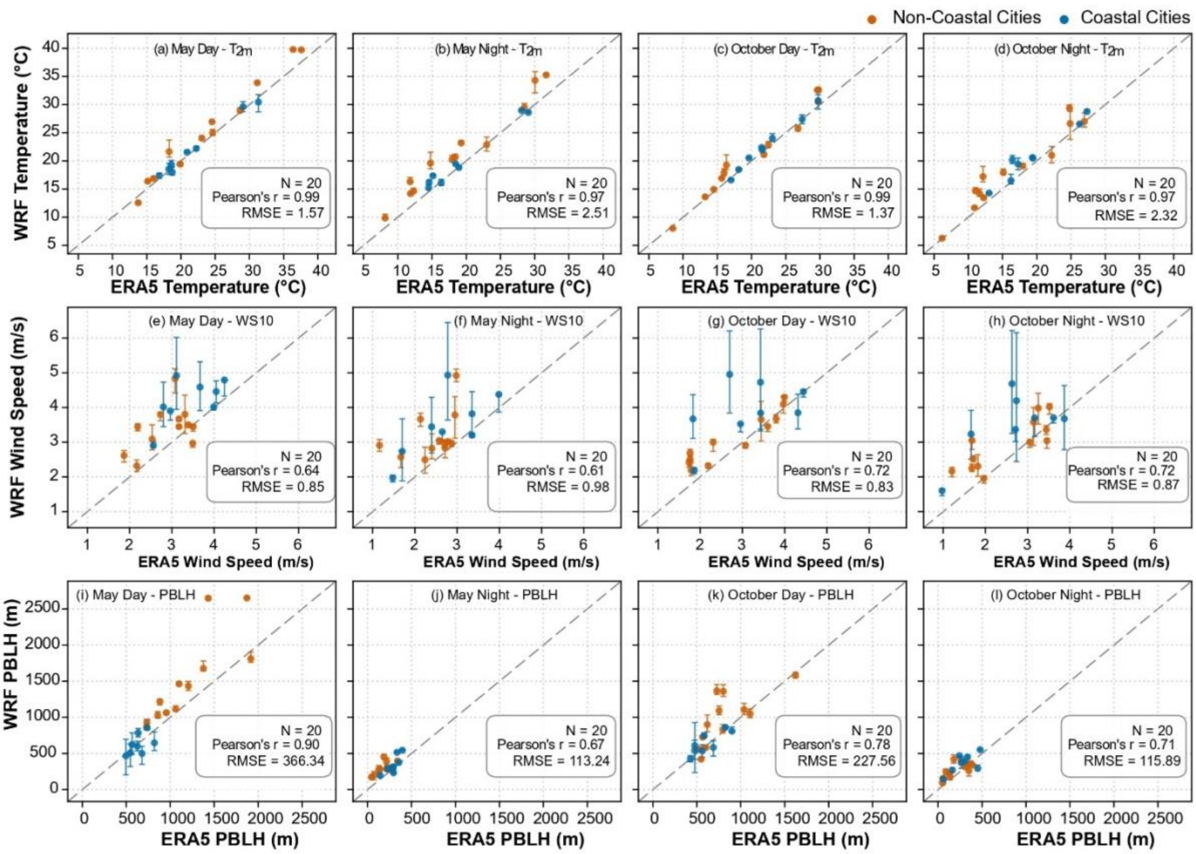

Figure S1: Comparison of WRF-simulated urban-core meteorology with ERA5 for the 20 megacities. Columns show May daytime, May nighttime, October daytime, and October nighttime, and rows show T, WS, and PBLH. ERA5 values are taken from the nearest grid point to the city-centre coordinate, whereas WRF values are averaged over the inner four radial rings (0-20 km radius) to achieve a broadly comparable spatial scale. Vertical error bars denote the WRF interquartile range (p25-p75) and colours distinguish non-coastal and coastal cities. Insets show the sample size, Pearson's correlation coefficient, and RMSE for each panel.

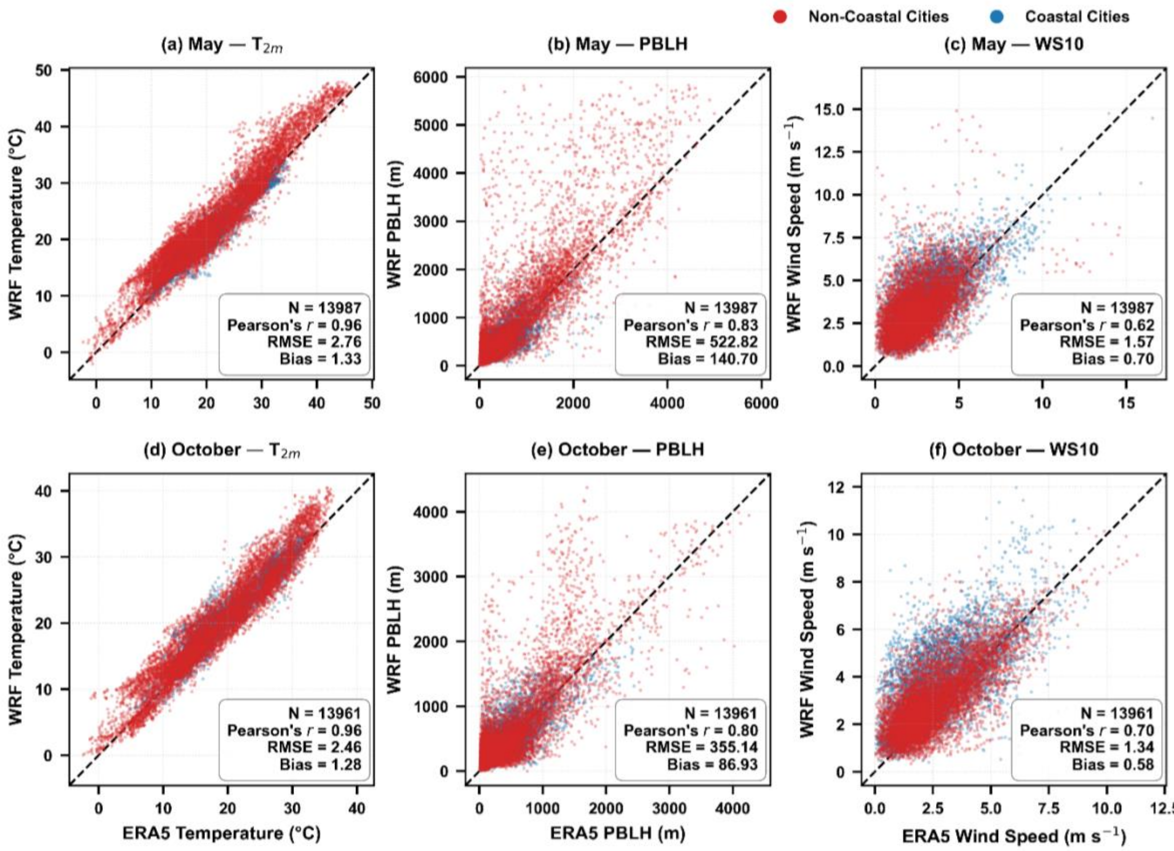

Figure S2: Hourly evaluation of WRF against ERA5 for May 2024 and October 2024. Scatter plots compare hourly city-scale WRF values (y-axis) with ERA5 values extracted from the nearest grid point to each city centre (x-axis) for (a, d) T, (b, e) PBLH, and (c, f) WS The top row shows May and the bottom row shows October. Red and blue points denote non-coastal and coastal cities, respectively. WRF values represent the spatial mean over the inner 0-20 km urban-core region, while ERA5 values are taken from the nearest 0.25° × 0.25° reanalysis grid cell. The dashed 1:1 line indicates perfect agreement. Each panel also reports the number of matched hourly samples (N), Pearson correlation coefficient (r), root mean square error (RMSE), and mean bias (WRF − ERA5).

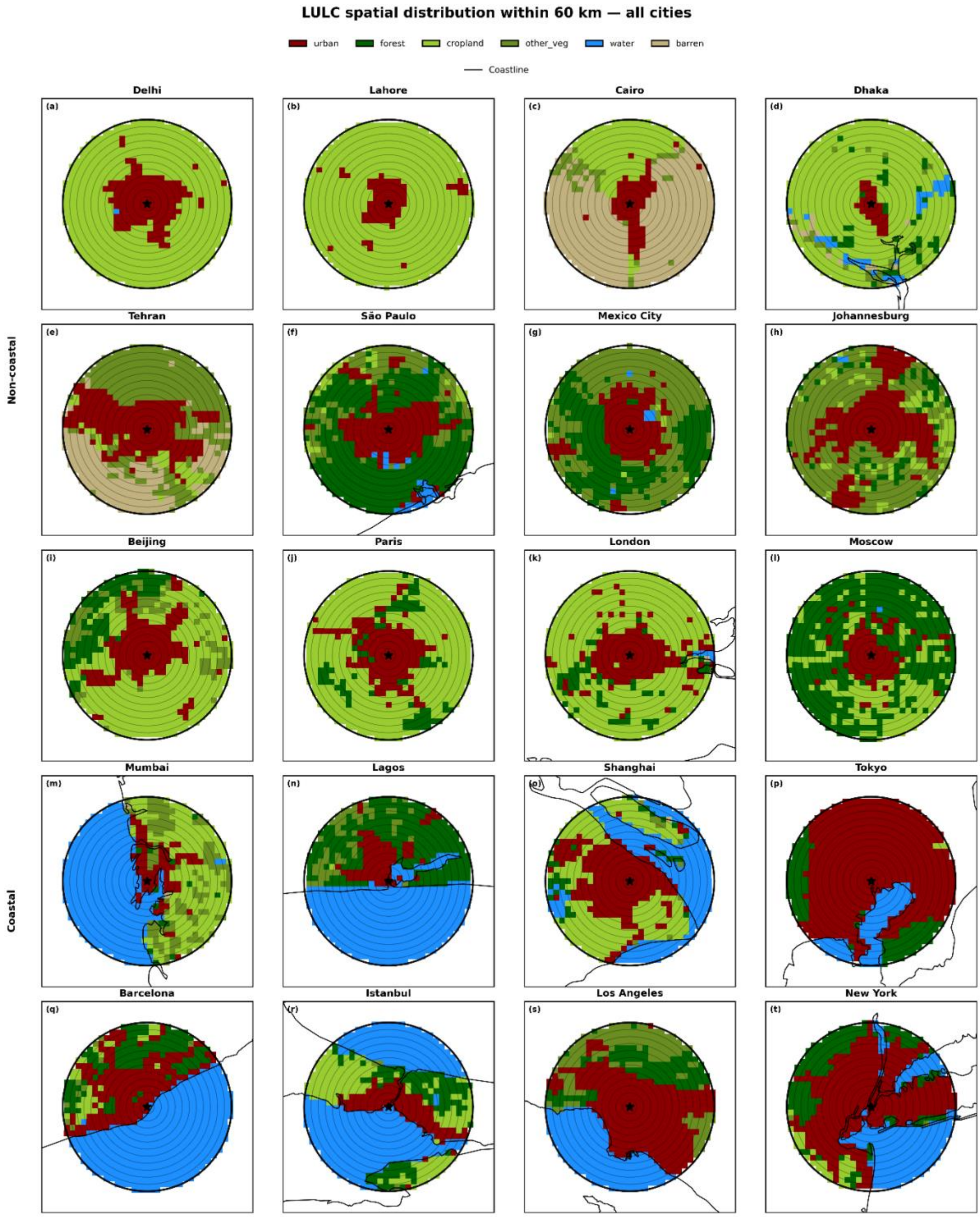

Figure S3: Azimuthal land-use/land-cover (LULC) distribution within the 60 km radial domain for all 20 megacities. Each panel shows the spatial arrangement of dominant LULC classes around the city centre (star), grouped into non-coastal and coastal cities. Concentric circles indicate 5 km radial intervals from the city centre to 60 km, and coastlines are overlaid where relevant. Colours denote the major LULC classes used in the analysis: urban, forest, cropland, other vegetation, water, and barren land. The figure highlights the strong azimuthal heterogeneity of the surrounding reference environment, particularly in coastal cities where land–water contrasts are pronounced and in terrain- or vegetation-complex inland cities where non-urban sectors are unevenly distributed.

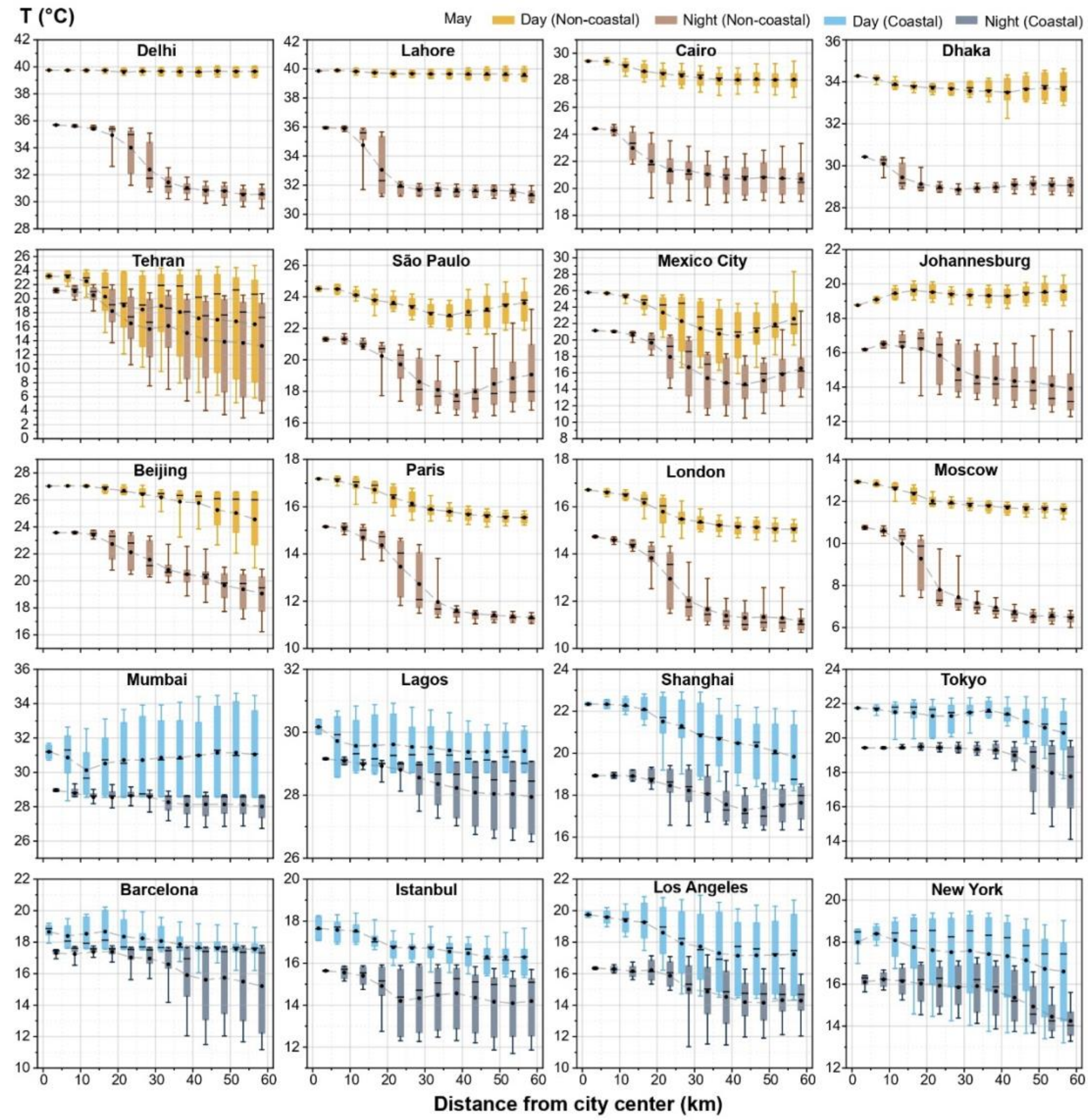

Figure S4: Radial distributions of T across the 20 megacities for May. Each city panel shows T statistics in 5 km radial bands from the city centre to 60 km, with non-coastal cities arranged in the upper three rows and coastal cities in the lower two rows. Daytime and nighttime distributions are shown separately, with colours distinguishing day and night for the two city groups. Boxes represent the interquartile range (p25-p75), whiskers represent p10-p90, and black markers connected by dashed lines indicate the ring-wise mean. Note that the y-axis temperature ranges vary across individual city panels to accommodate distinct local thermal amplitudes. The visual density of the horizontal gridlines directly reflects the magnitude of the temperature range in each city. The identical city order and panel arrangement in both months allow direct comparison of the radial thermal structure under contrasting seasonal conditions.

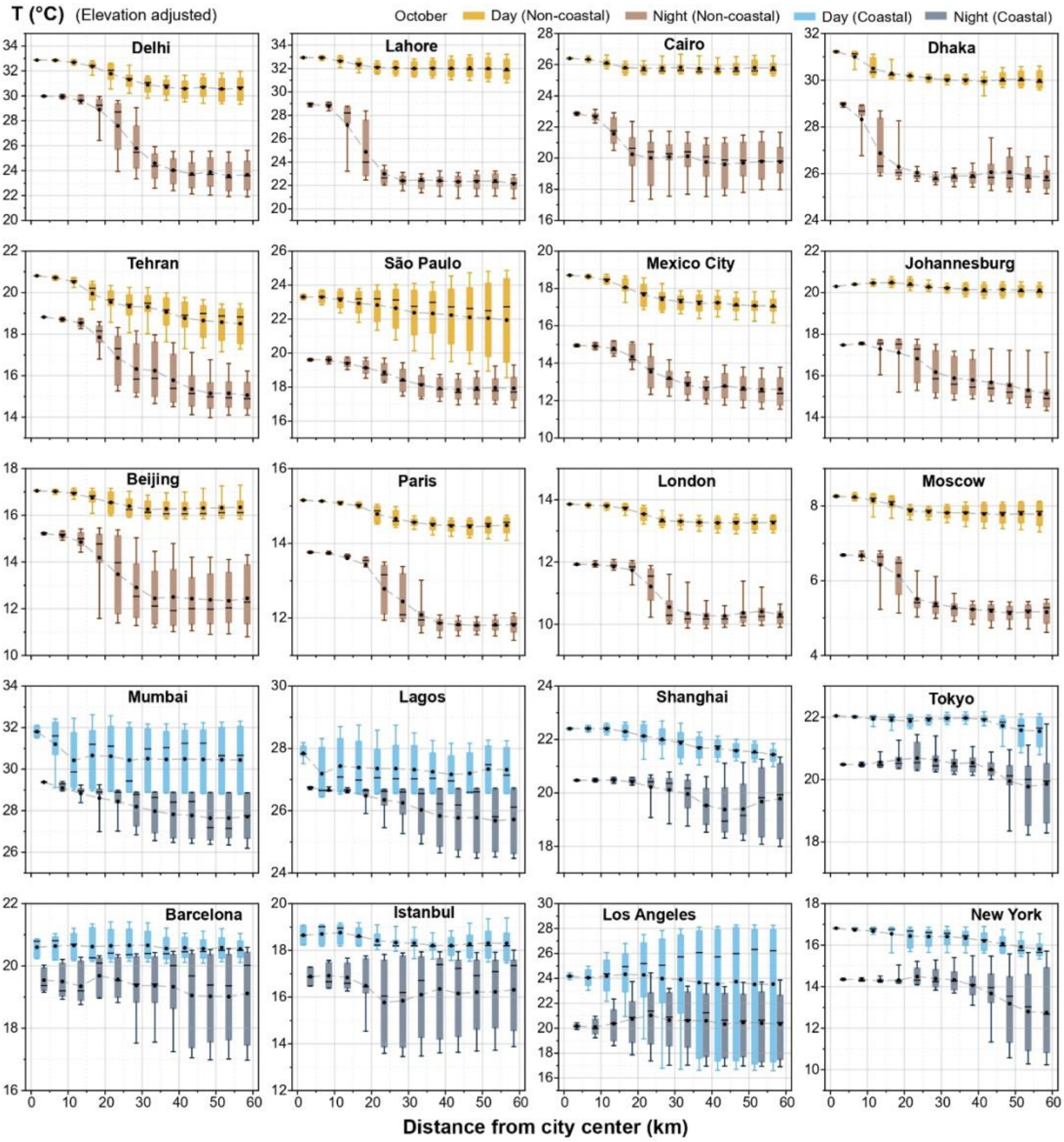

Figure S5: Elevation-adjusted T radial distributions for all megacities in October 2024. Panels show ring-wise distributions of after applying a grid-level elevation adjustment prior to radial aggregation, in which each grid-cell temperature was adjusted to a common city-specific reference height using a constant environmental lapse rate of 6.5 K km s^{-1}. The reference height was defined from the urban-core elevation, and the adjusted temperature field was then aggregated into 5 km concentric rings from the city centre to 60 km. Results are shown separately for daytime and nighttime composites and grouped into non-coastal and coastal cities. Boxes indicate the interquartile range (p2-p75), whiskers show p10-p90, horizontal lines denote the median, and black dots mark the mean for each ring.

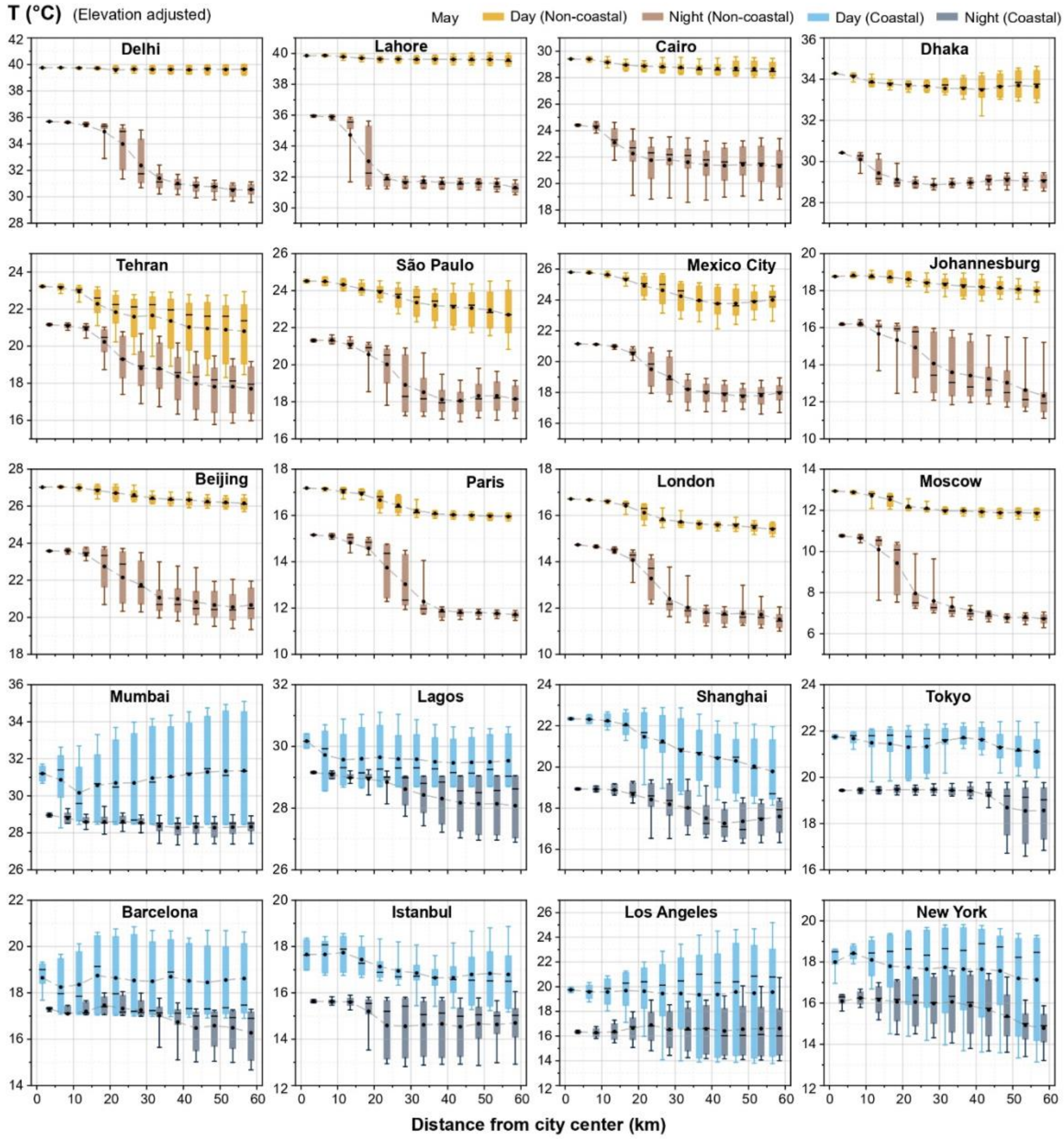

Figure S6: Elevation-adjusted T radial distributions for all megacities in May 2024. Panels show ring-wise distributions of T after applying a grid-level elevation adjustment prior to radial aggregation, in which each grid-cell temperature was normalized to a common city-specific reference height using a constant environmental lapse rate of 6.5 K km s^{-1}.

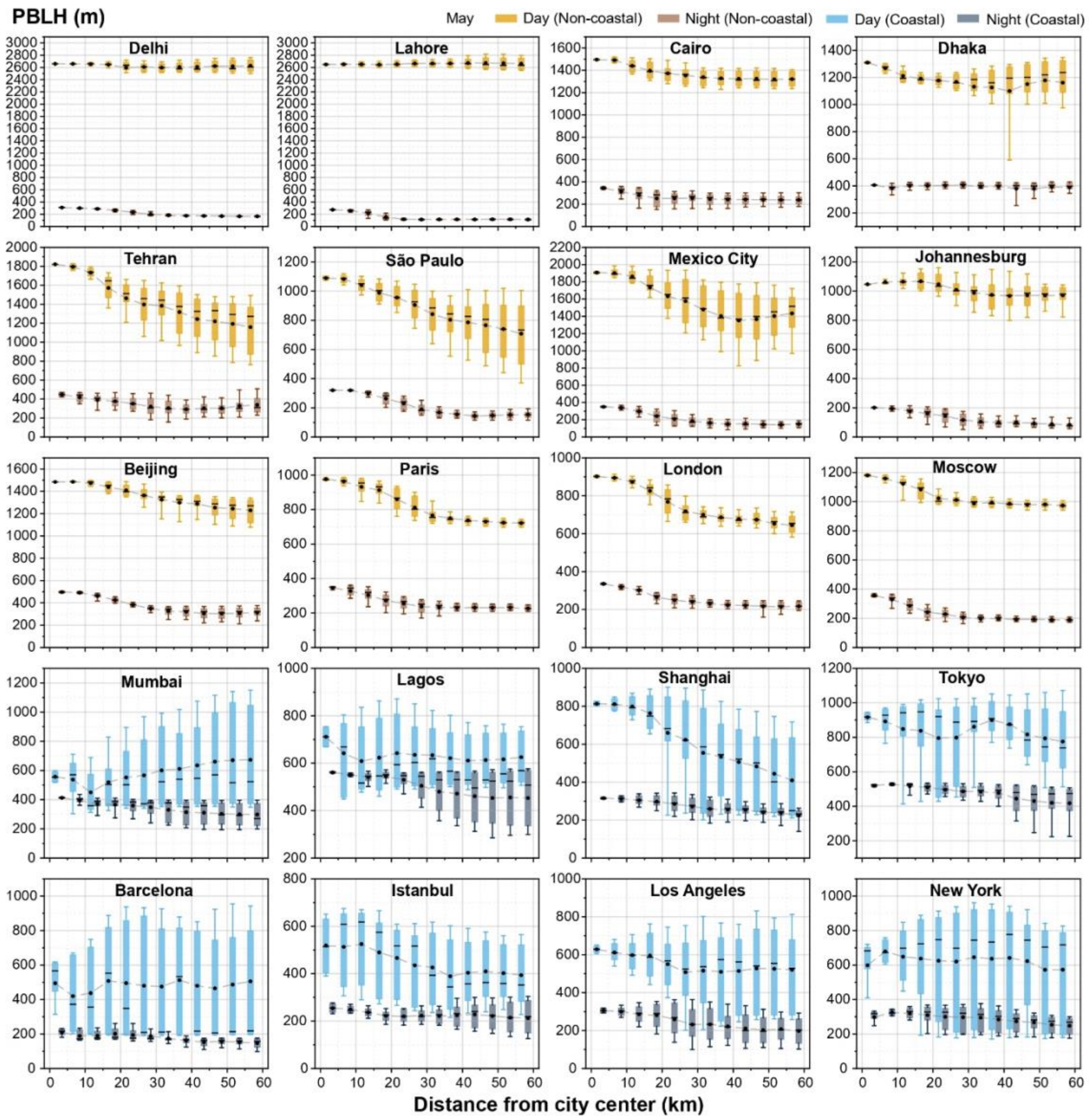

Figure S7: May. Each city panel shows PBLH statistics in 5 km radial bands from the city centre to 60 km, with non-coastal cities arranged in the upper three rows and coastal cities in the lower two rows. Daytime and nighttime distributions are shown separately, with colours distinguishing day and night for the two city groups. Boxes represent the interquartile range (p25-p75), whiskers represent p10-p90, and black markers connected by dashed lines indicate the ring-wise mean.

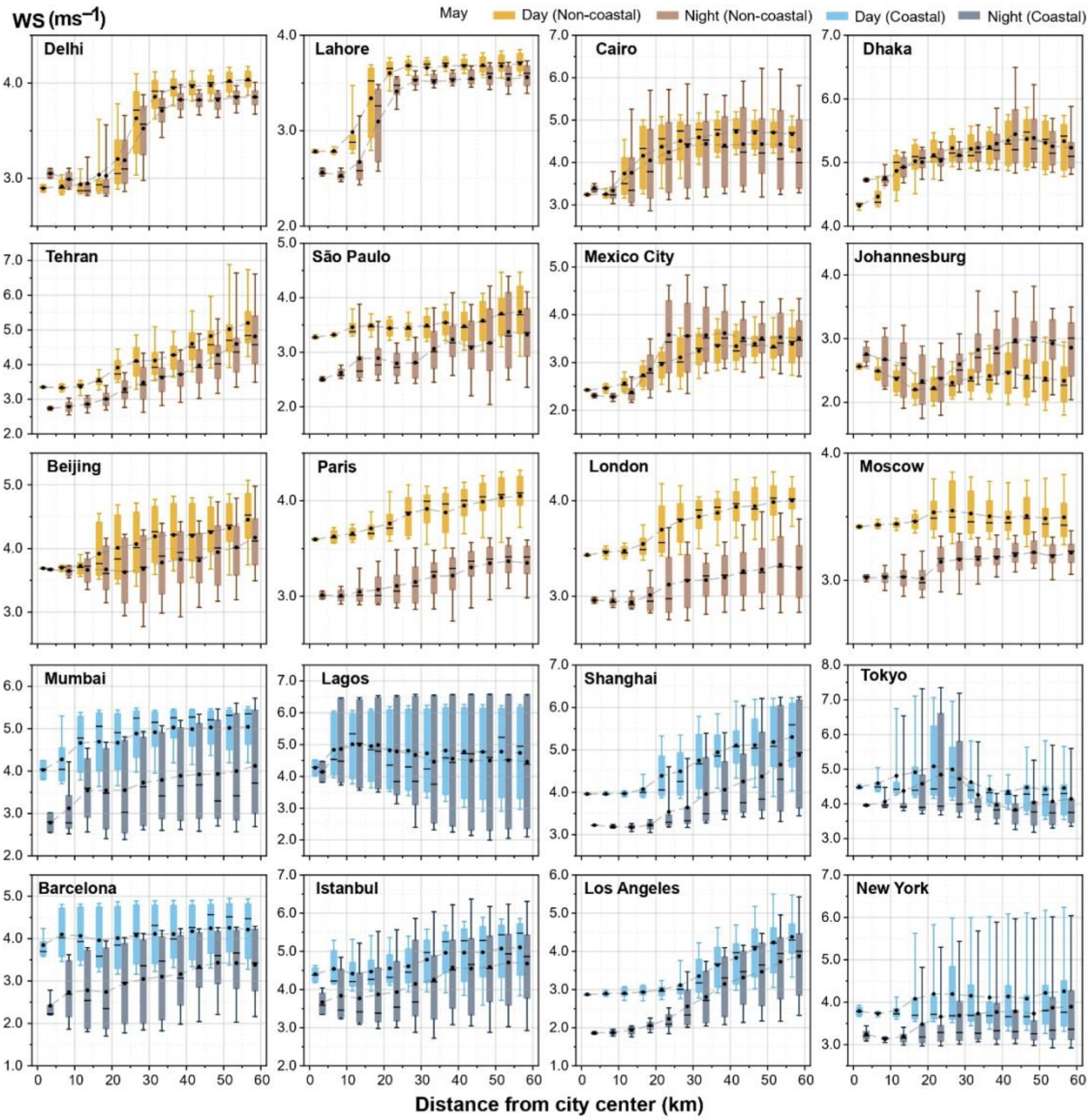

Figure S8: Radial distributions of WS10 across the 20 megacities for May. Each city panel shows WS10 statistics in 5 km radial bands from the city centre to 60 km, with non-coastal cities arranged in the upper three rows and coastal cities in the lower two rows. Daytime and nighttime distributions are shown separately, with colours distinguishing day and night for the two city groups. Boxes represent the interquartile range (p25-p75), whiskers represent p10-p90, and black markers connected by dashed lines indicate the ring-wise mean.

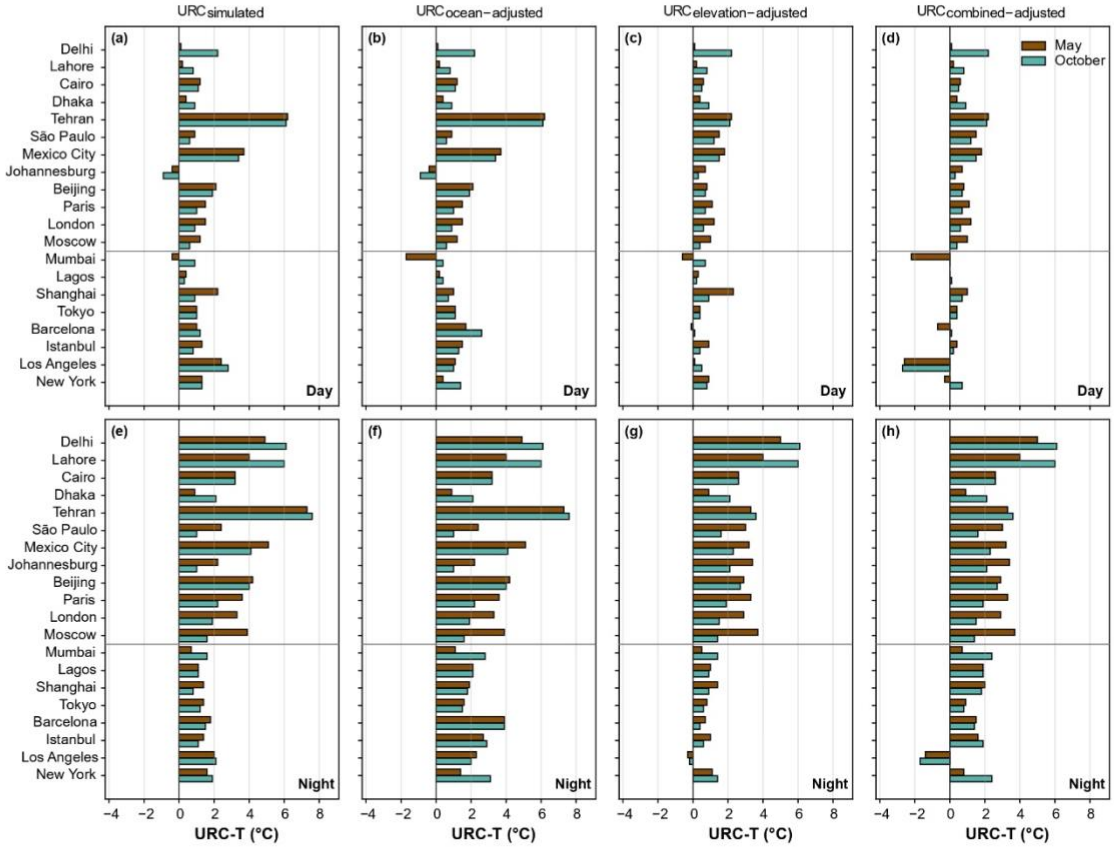

Figure S9: Diagnosed Urban-Radial Contrast (URC) in near-surface 2 m temperature (URC-T) at each of the four analysis states defined in Sect. 2.7: simulated (a, e), ocean-adjusted (b, f), elevation-adjusted (c, g), and combined-adjusted (d, h), for daytime (a-d) and nighttime (e-h) conditions. Bars show May (brown) and October (teal) values for each of the twenty cities, grouped into twelve non-coastal (upper) and eight coastal (lower) cities, separated by the horizontal line. Because land-only masking (ocean adjustment) was not applied to non-coastal cities, their simulated and ocean-adjusted values (a versus b, e versus f) are identical, as are their elevation-adjusted and combined-adjusted values (c versus d, g versus h); any difference between columns for non-coastal cities therefore reflects the elevation-attributed component alone. For coastal cities, all four states can differ, reflecting the combined influence of the ocean- and elevation-attributed components.

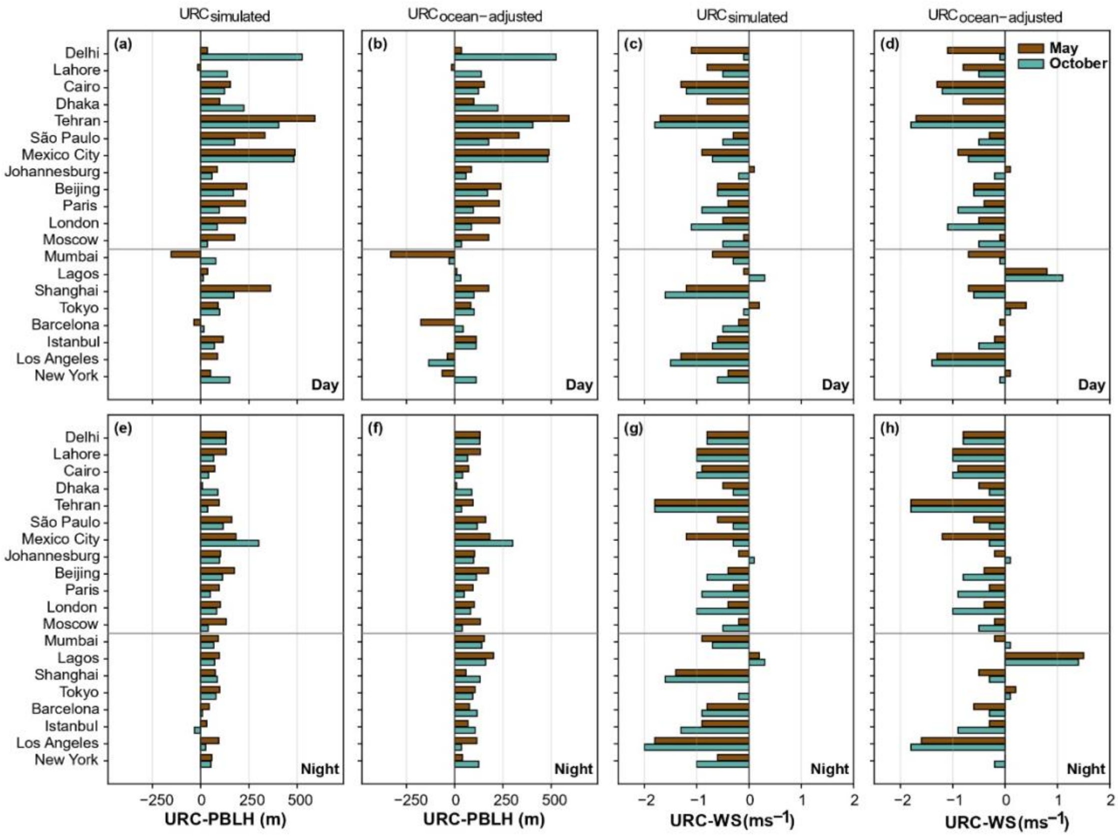

Figure S10: Diagnosed Urban-Radial Contrast (URC) in planetary boundary layer height (URC-PBLH; a, b, e, f) and 10 m wind speed (URC-WS; c, d, g, h) at the simulated (a, c, e, g) and ocean-adjusted (b, d, f, h) analysis states, for daytime (a-d) and nighttime (e-h) conditions. As no elevation adjustment is applied to these variables (Sect. 2.7), only two analysis states are shown, in contrast to the four shown for URC-T (Fig. S9). Bars show May (brown) and October (teal) values for each of the twenty cities, grouped into twelve non-coastal (upper) and eight coastal (lower) cities, separated by the horizontal line. Because land-only masking was not applied to non-coastal cities, their simulated and ocean-adjusted values are identical in every panel; for coastal cities, the difference between the two corresponds to the ocean-attributed component

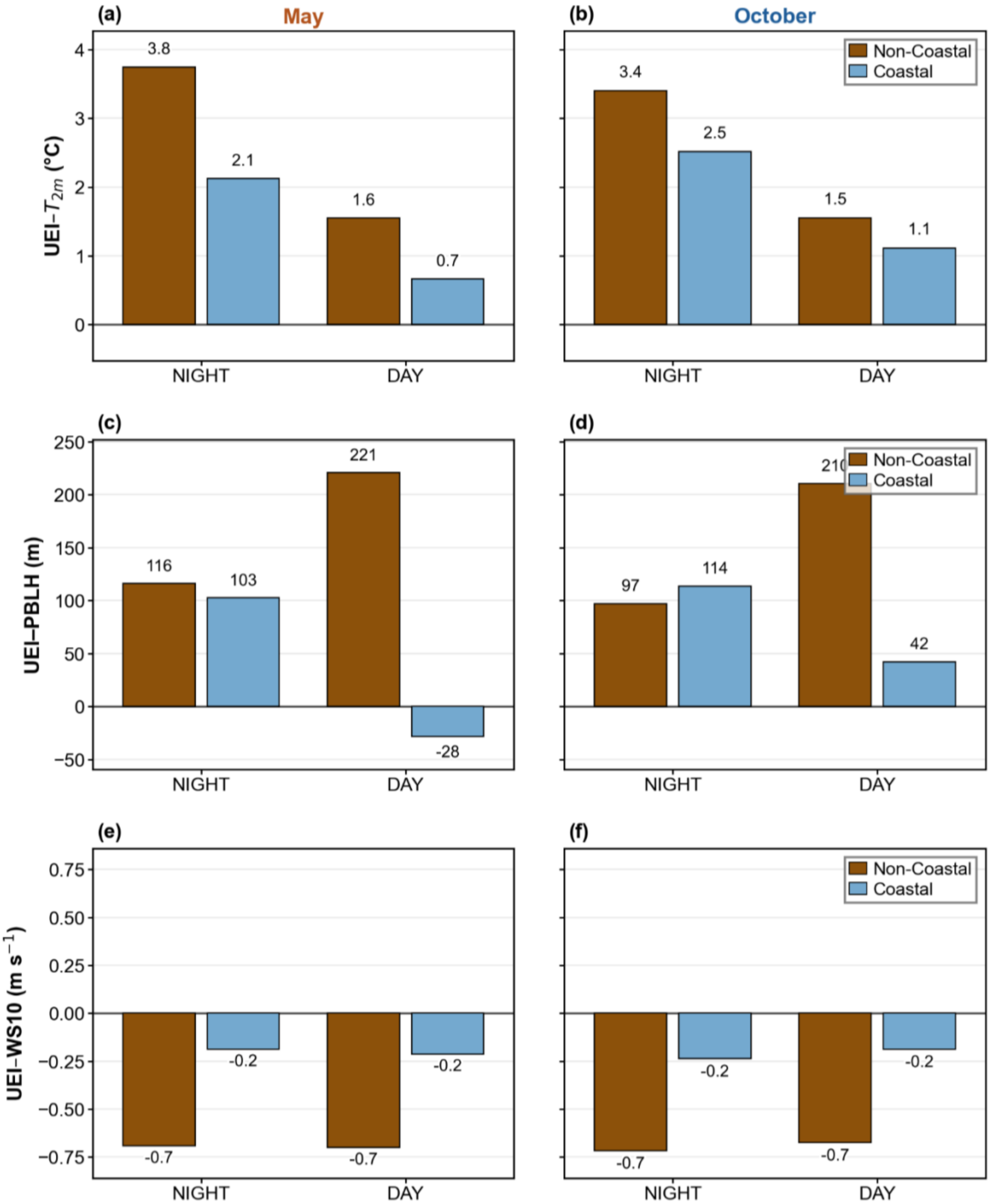

Figure S11: Category-grouped Urban Radial Contrast (URC) after applying land-only masking in coastal cities. Panels (a, b) show URC-T, panels (c, d) show URC-PBLH, and panels (e, f) show URC-WS. Results are grouped by season (May: left column; October: right column), city type (non-coastal: brown; coastal: blue), and time of day (night and day). For non-coastal cities, grouped means are unchanged from the simulated analysis, whereas for coastal cities, the grouped means are recalculated after excluding ocean grid cells from the radial domain. Positive URC values indicate urban enhancement relative to the outer reference, while negative values indicate urban reduction. The figure highlights how land-water sampling modifies the grouped coastal response.

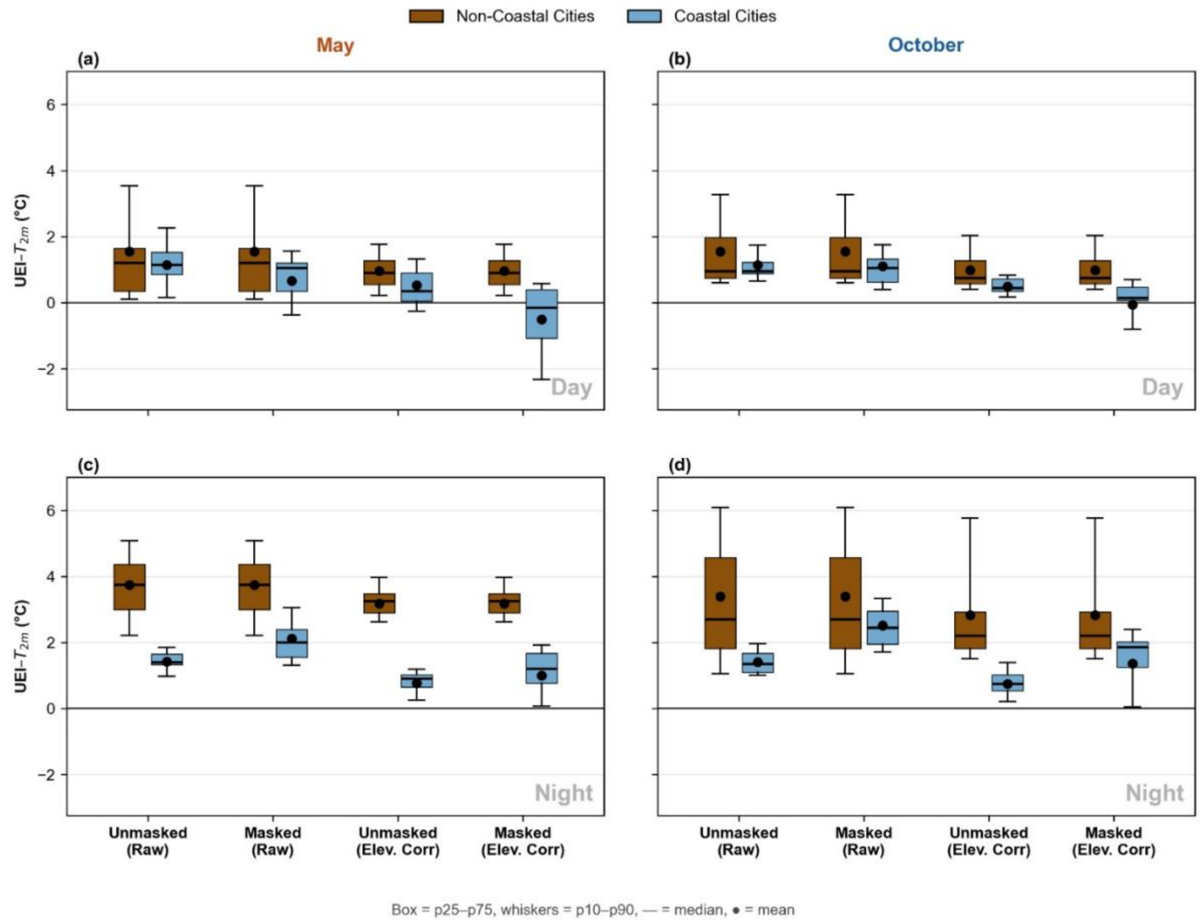

Figure S12: Distribution of the diagnosed Urban-Radial Contrast (URC) in near-surface temperature (URC-T) for non-coastal (brown, n=12) and coastal (blue, n=8) cities, at each of the four analysis states defined in Sect. 2.7 (simulated, ocean-adjusted, elevation-adjusted, and combined-adjusted), for daytime (a, b) and nighttime (c, d) conditions in May (a, c) and October (b, d). Boxes show the 25th-75th percentile range, whiskers show the 10th-90th percentile range, horizontal lines mark the median, and filled circles mark the mean across cities within each group. Because land-only masking (ocean adjustment) was not applied to non-coastal cities, their distributions are identical between the simulated and ocean-adjusted states, and between the elevation-adjusted and combined-adjusted states; only the coastal group's distribution changes across all four states.

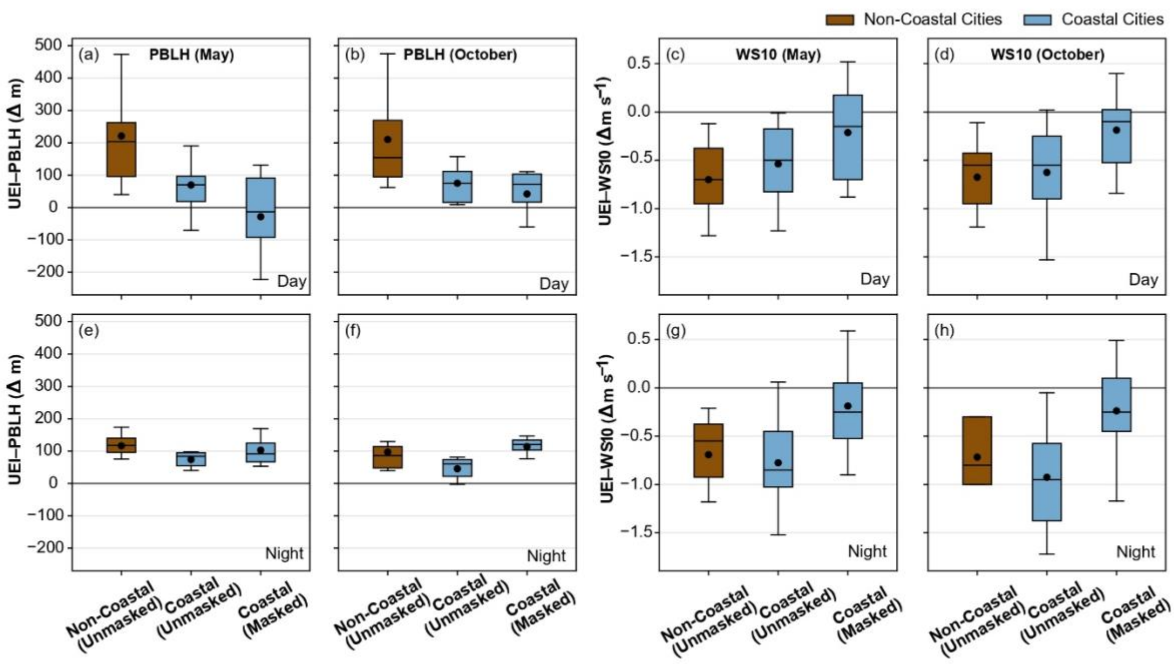

Figure S13: Distribution of the diagnosed Urban-Radial Contrast (URC) in planetary boundary layer height (URC-PBLH; a, b, e, f) and 10 m wind speed (URC-WS; c, d, g, h) for non-coastal (brown, n=12) and coastal (blue, n=8) cities, at each of the four analysis states defined in Sect. 2.7, for daytime (a-d) and nighttime (e-h) conditions in May (a, c, e, g) and October (b, d, f, h). Because no elevation adjustment applies to these variables (Sect. 2.7), only two analysis states are shown per group: simulated for non-coastal cities, and both simulated and ocean-adjusted for coastal cities, for which land-only masking (ocean adjustment) was required. Boxes show the 25th-75th percentile range, whiskers show the 10th-90th percentile range, horizontal lines mark the median, and filled circles mark the mean across cities within each group.

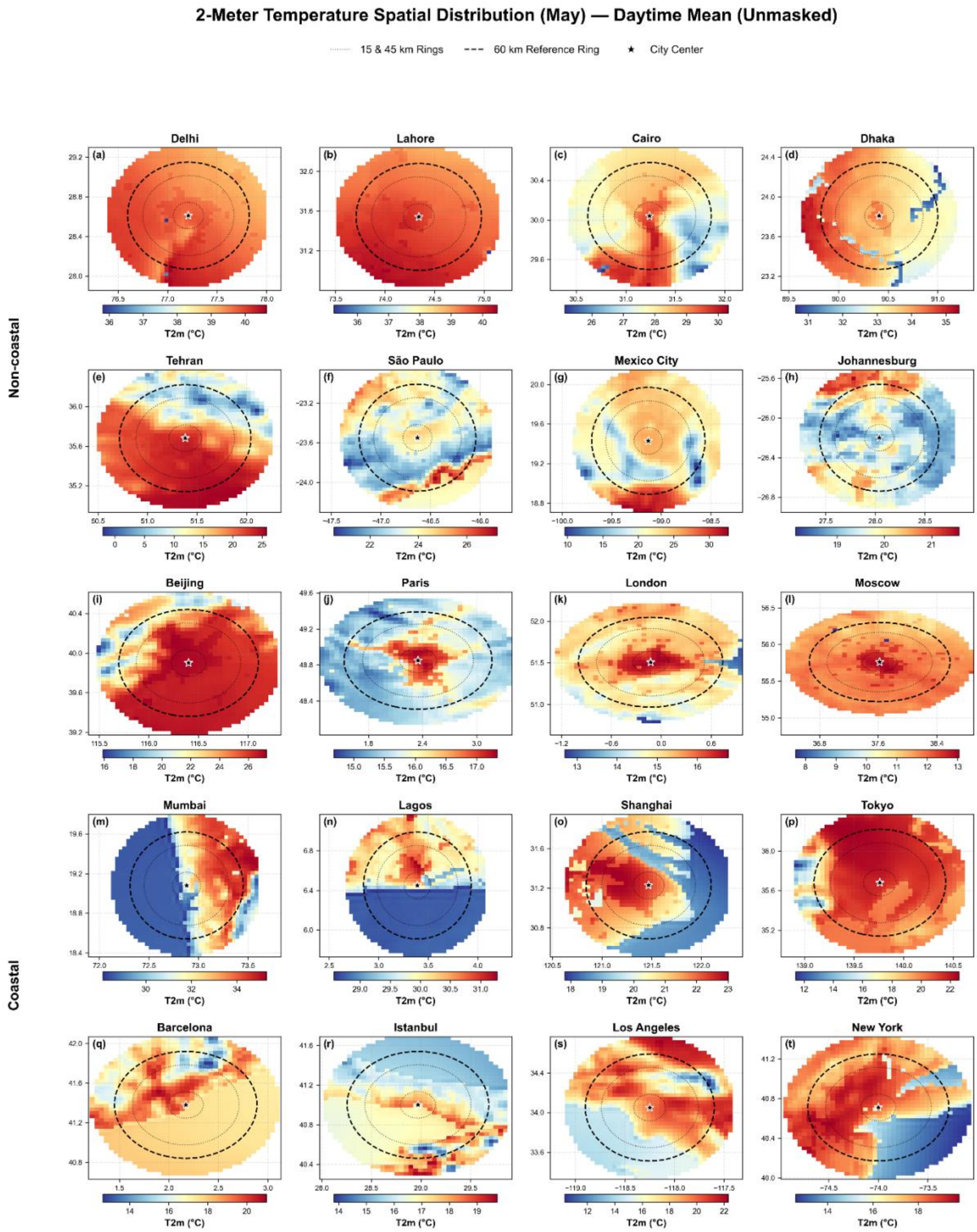

Figure S*14*: Spatial distribution of daytime mean near-surface air temperature (T) for May 2024 obtained from the Simulated (prior to any adjustment) WRF simulations for the twenty study cities. Cities are grouped into non-coastal (top three rows) and coastal (bottom two rows) categories. The star marks the city centre, while the concentric circles indicate the 15 km urban-core boundary (dotted), the 45 km outer urban boundary (dotted), and the 60 km reference radius (dashed) adopted for the radial analysis and Urban Effect Intensity (UEI) calculations. An independent colour scale is applied to each city to preserve the spatial temperature variability within individual domains; consequently, colours should be interpreted within each panel rather than compared directly between cities.

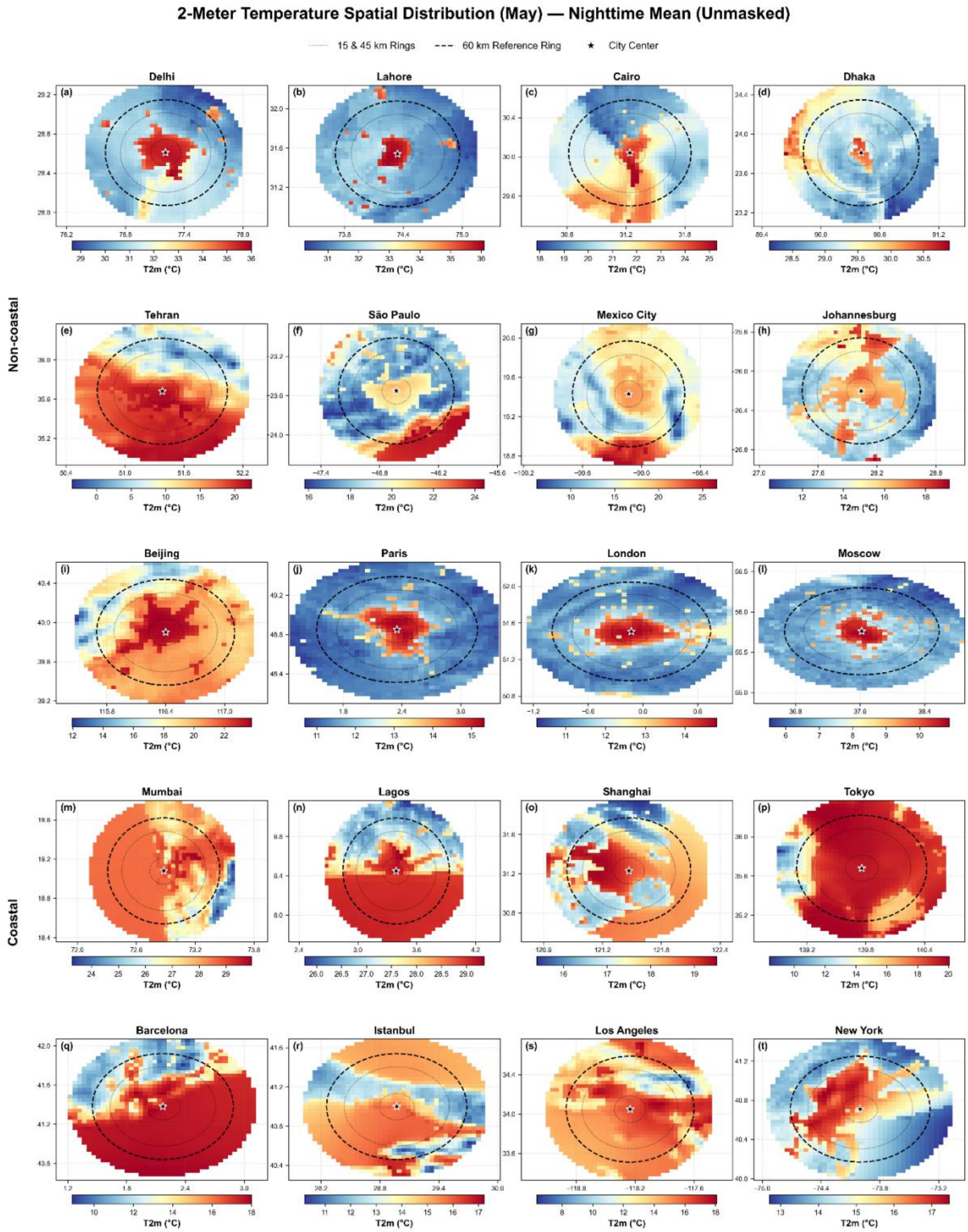

Figure S15: Spatial distribution of nighttime mean near-surface air temperature (T) for May 2024 obtained from the Simulated (prior to any adjustment) WRF simulations for the twenty study cities. Cities are grouped into non-coastal (top three rows) and coastal (bottom two rows) categories. The star marks the city centre, while the concentric circles indicate the 15 km urban-core boundary (dotted), the 45 km outer urban boundary (dotted), and the 60 km reference radius (dashed) adopted for the radial analysis and Urban Effect Intensity (UEI) calculations. An independent colour scale is applied to each city to preserve the spatial temperature variability within individual domains; consequently, colours should be interpreted within each panel rather than compared directly between cities.

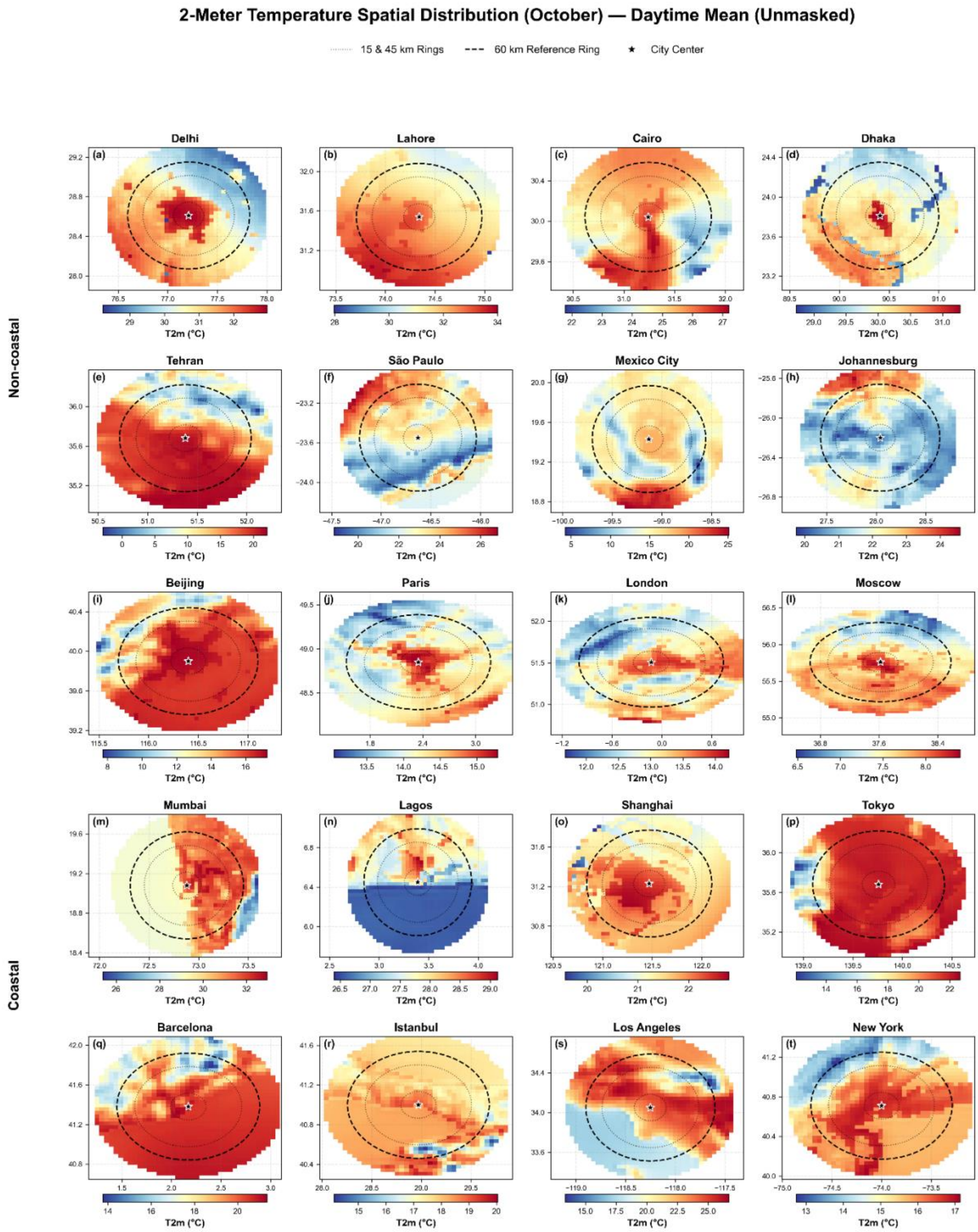

Figure S*16*: Spatial distribution of daytime mean near-surface air temperature (T) for October 2024 obtained from the Simulated (prior to any adjustment) WRF simulations for the twenty study cities. Cities are grouped into non-coastal (top three rows) and coastal (bottom two rows) categories. The star marks the city centre, while the concentric circles indicate the 15 km urban-core boundary (dotted), the 45 km outer urban boundary (dotted), and the 60 km reference radius (dashed) adopted for the radial analysis and Urban Effect Intensity (UEI) calculations. An independent colour scale is applied to each city to preserve the spatial temperature variability within individual domains; consequently, colours should be interpreted within each panel rather than compared directly between cities.

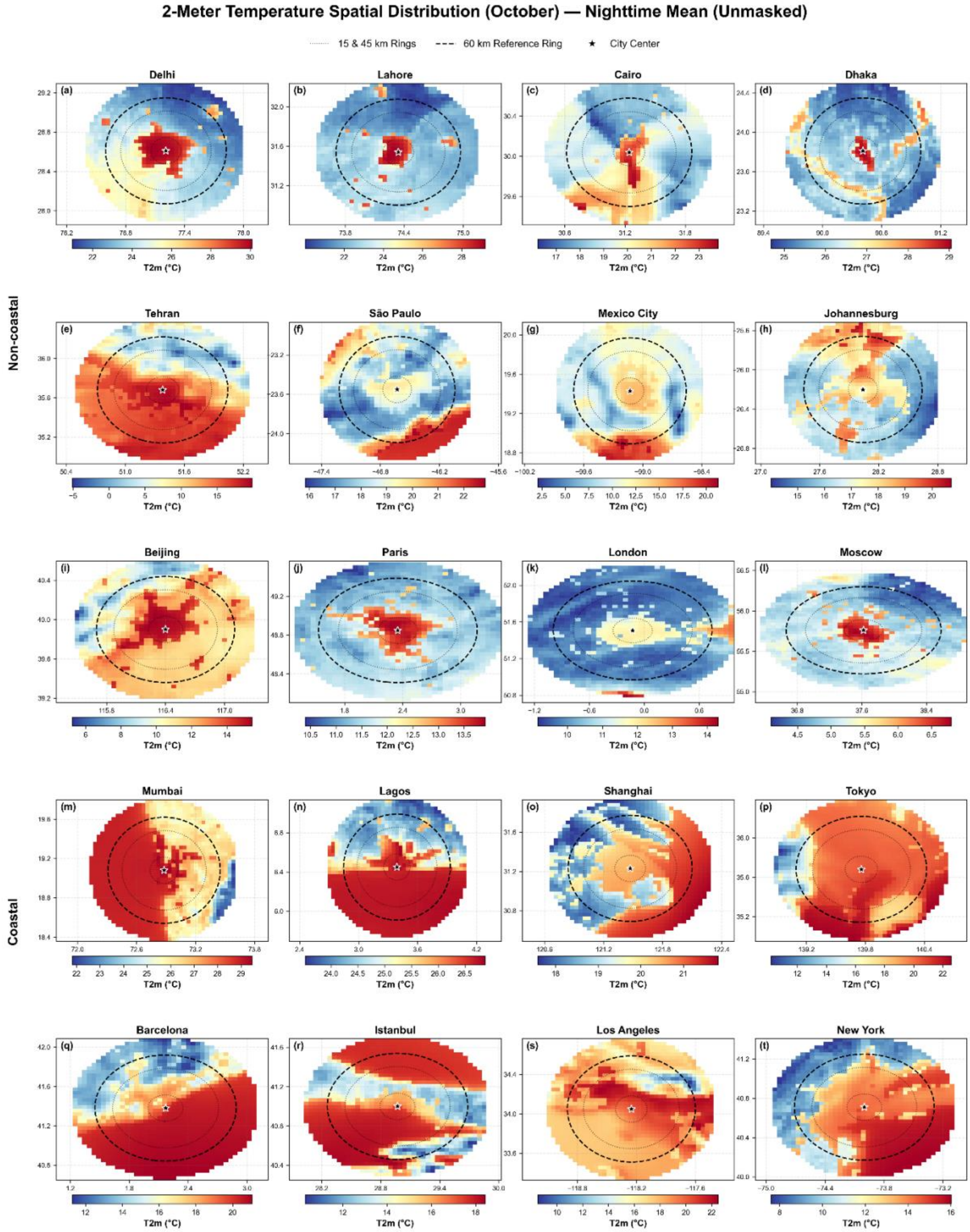

Figure S*17*: Spatial distribution of nighttime mean near-surface air temperature (T) for October 2024 obtained from the Simulated (prior to any adjustment) WRF simulations for the twenty study cities. Cities are grouped into non-coastal (top three rows) and coastal (bottom two rows) categories. The star marks the city centre, while the concentric circles indicate the 15 km urban-core boundary (dotted), the 45 km outer urban boundary (dotted), and the 60 km reference radius (dashed) adopted for the radial analysis and Urban Effect Intensity (UEI) calculations. An independent colour scale is applied to each city to preserve the spatial temperature variability within individual domains; consequently, colours should be interpreted within each panel rather than compared directly between cities.

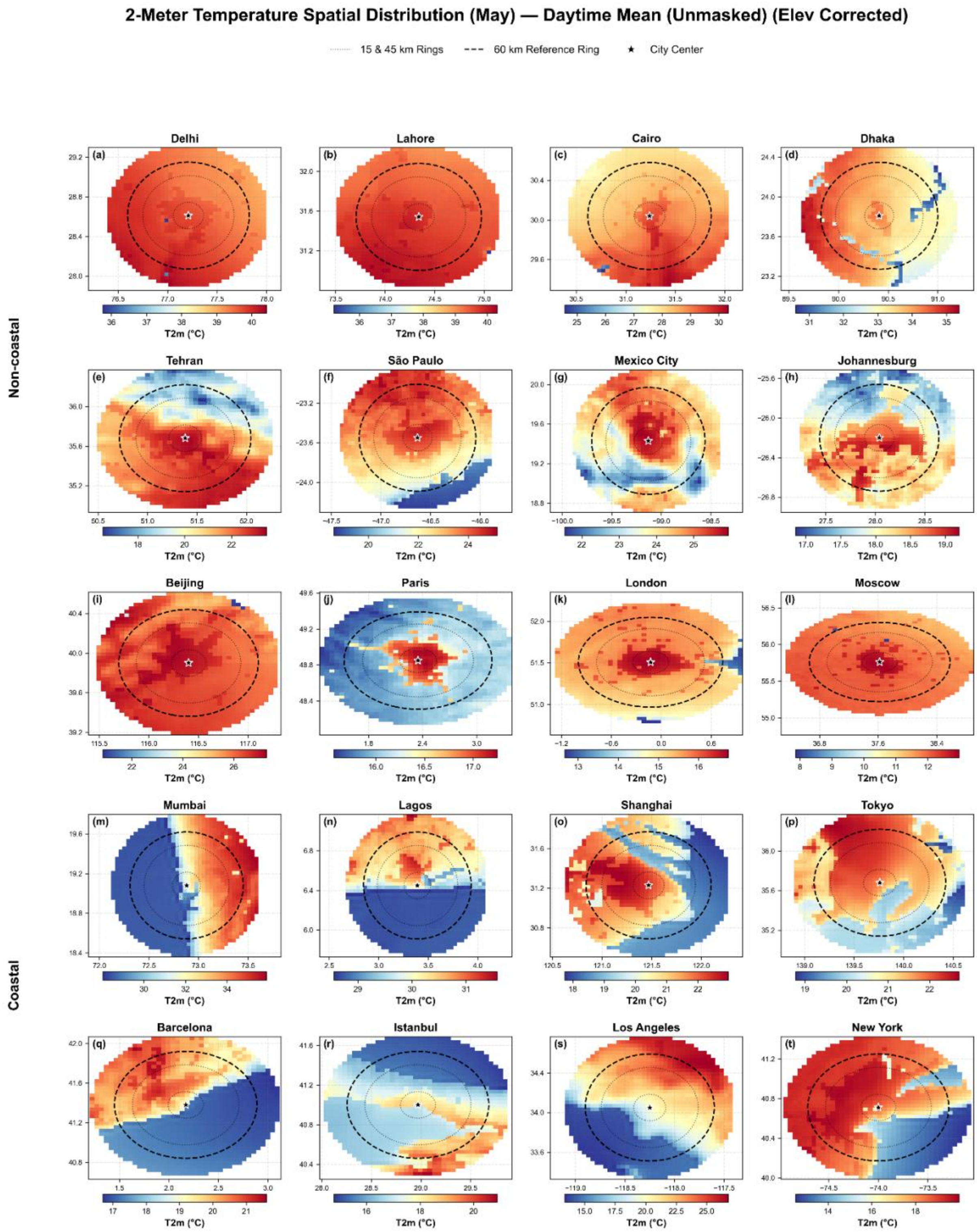

Figure S*18*: Spatial distribution of elevation-adjusted daytime mean near-surface air temperature (T) for May 2024 across the twenty study cities. The original WRF-simulated T fields were adjusted to a common reference elevation for each city using the environmental lapse-rate approach described in Sect. 2.7 to minimise temperature differences arising solely from variations in terrain height. Cities are grouped into non-coastal (top three rows) and coastal (bottom two rows) categories. The white star marks the city centre, while the concentric circles indicate the 15 km urban-core boundary (dotted), the 45 km outer urban boundary (solid), and the 60 km reference radius (dashed) adopted for the radial analysis and Urban

Effect Intensity (UEI) calculations. An independent colour scale is used for each city to preserve the spatial temperature variability within individual domains; therefore, colours should be interpreted only within each panel and not compared quantitatively between different cities.

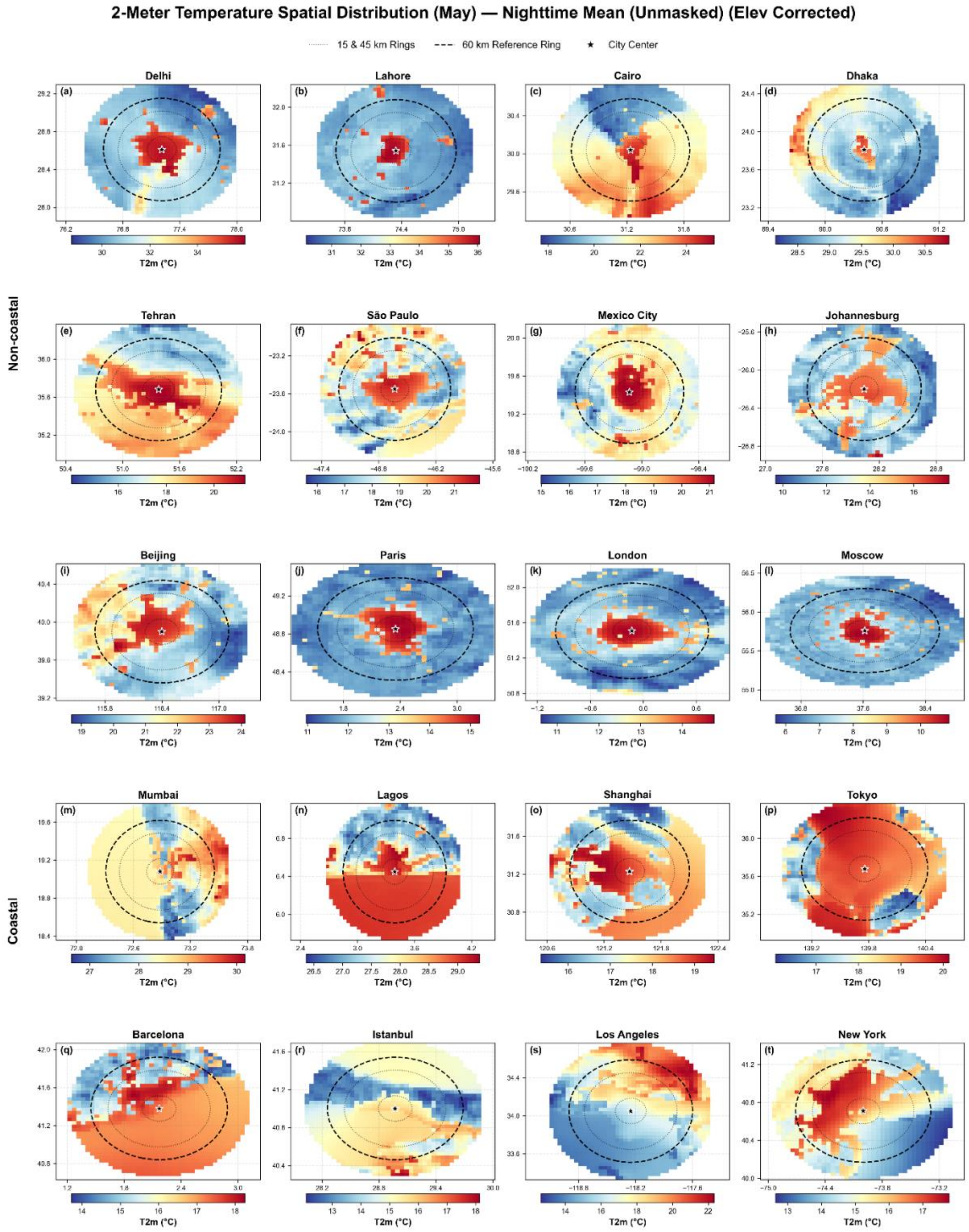

Figure S19: Spatial distribution of elevation-adjusted nighttime mean near-surface air temperature (T) for May 2024 across the twenty study cities. The original WRF-simulated T fields were adjusted to a common reference elevation for each city using the environmental lapse-rate approach described in Sect. 2.7 to minimise temperature differences arising solely from variations in terrain height. Cities are grouped into non-coastal (top three rows) and coastal (bottom two rows) categories. The white star marks the city centre, while the concentric circles indicate the 15 km urban-core boundary (dotted), the 45 km outer urban boundary (solid), and the 60 km reference radius (dashed) adopted for the radial analysis and Urban Effect Intensity (UEI) calculations. An independent colour scale is used for each city to preserve the spatial temperature variability within individual domains; therefore, colours should be interpreted only within each panel and not compared quantitatively between different cities.

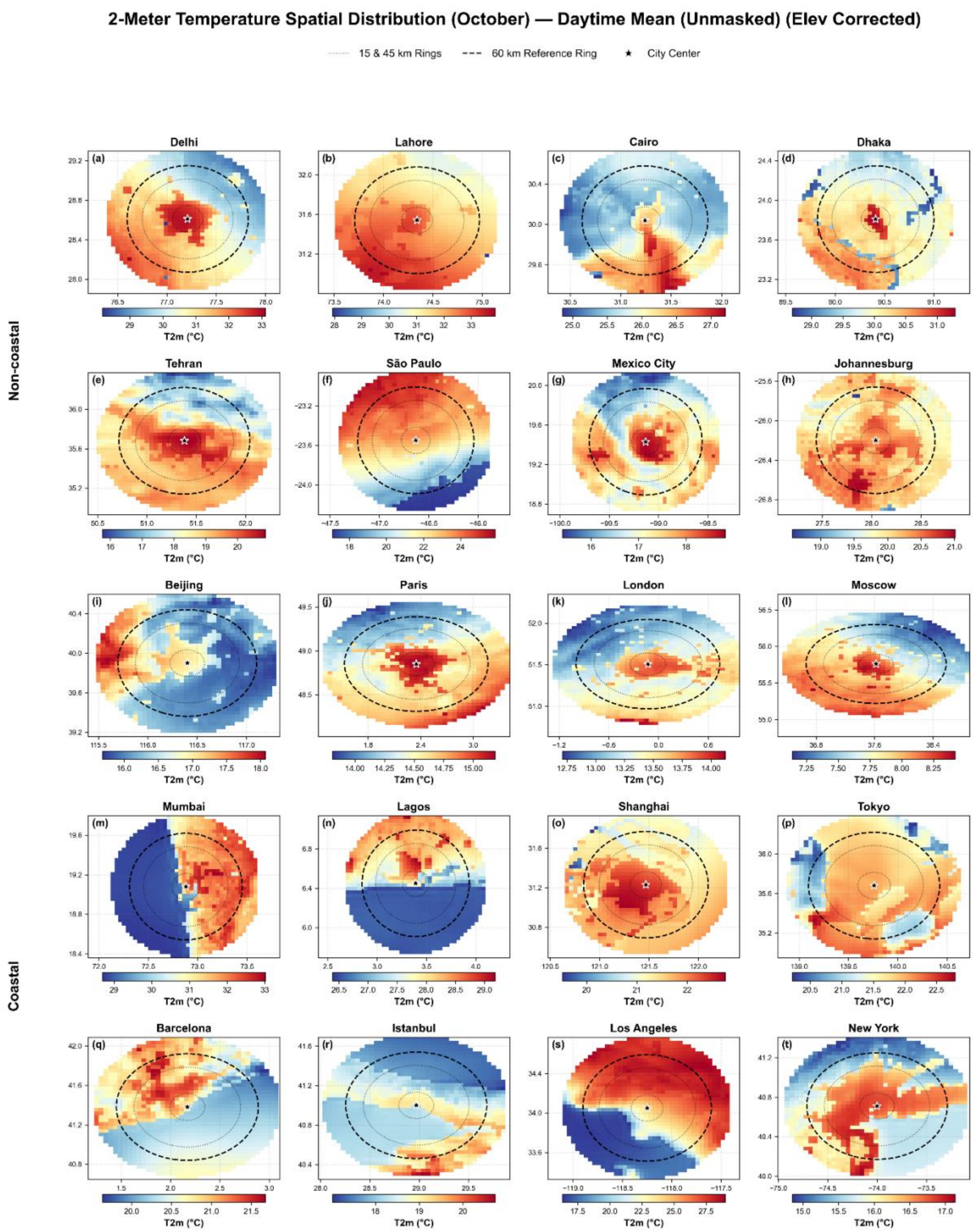

Figure S20: Spatial distribution of elevation-adjusted daytime mean near-surface air temperature (T) for October 2024 across the twenty study cities. The original WRF-simulated T fields were adjusted to a common reference elevation for each city using the environmental lapse-rate approach described in Sect. 2.7 to minimise temperature differences arising solely from variations in terrain height. Cities are grouped into non-coastal (top three rows) and coastal (bottom two rows) categories. The white star marks the city centre, while the concentric circles indicate the 15 km urban-core boundary (dotted), the 45 km outer urban boundary (solid), and the 60 km reference radius (dashed) adopted for the radial analysis and

Urban Effect Intensity (UEI) calculations. An independent colour scale is used for each city to preserve the spatial temperature variability within individual domains; therefore, colours should be interpreted only within each panel and not compared quantitatively between different cities.

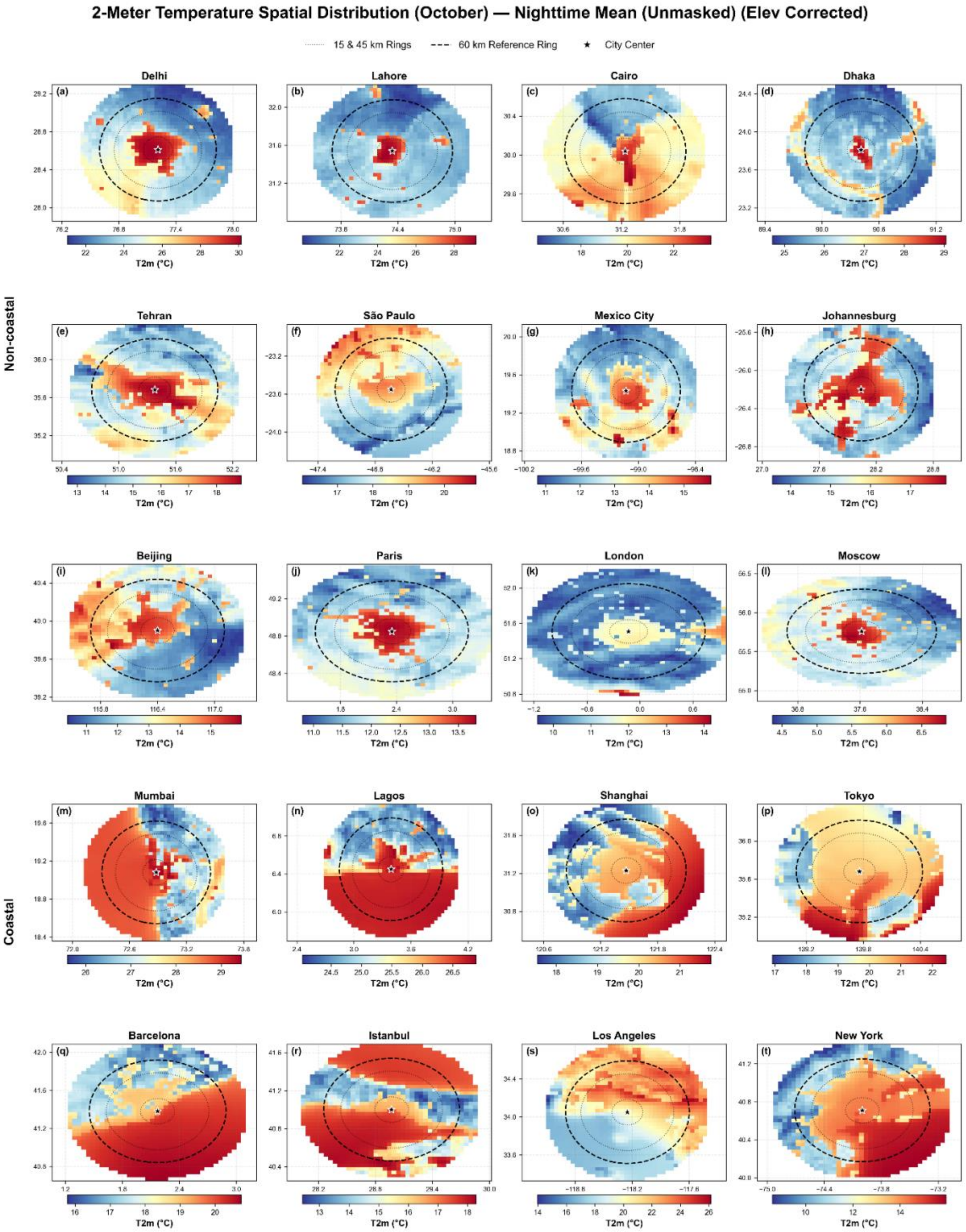

Figure S*21*: Spatial distribution of elevation-adjusted nighttime mean near-surface air temperature (T) for October 2024 across the twenty study cities. The original WRF-simulated T fields were adjusted to a common reference elevation for each city using the environmental lapse-rate approach described in Sect. 2.7 to minimise temperature differences arising solely from variations in terrain height. Cities are grouped into non-coastal (top three rows) and coastal (bottom two rows) categories. The white star marks the city centre, while the concentric circles indicate the 15 km urban-core boundary (dotted), the 45 km outer urban boundary (solid), and the 60 km reference radius (dashed) adopted for the radial analysis and Urban Effect Intensity (UEI) calculations. An independent colour scale is used for each city to preserve the spatial temperature variability within individual domains; therefore, colours should be interpreted only within each panel and not compared quantitatively between different cities.

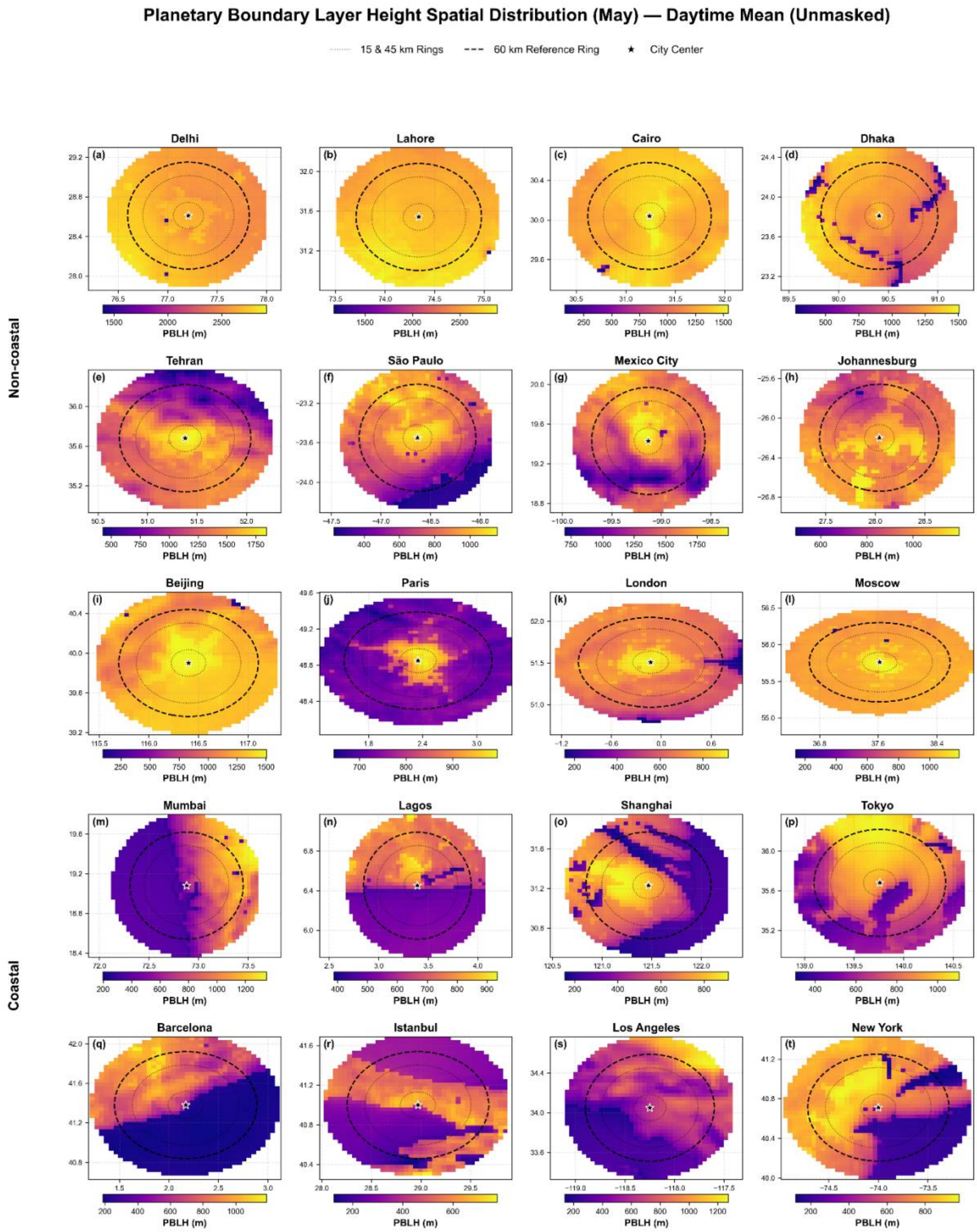

Figure S22: Spatial distribution of daytime mean planetary boundary layer height (PBLH) for May 2024 obtained from the Simulated WRF simulations for the twenty study cities. Cities are grouped into non-coastal (top three rows) and coastal (bottom two rows) categories. The star marks the city centre, while the concentric circles indicate the 15 km urban-core boundary (dotted), the 45 km outer urban boundary (solid), and the 60 km reference radius (dashed) adopted for the radial analysis and Urban Effect Intensity (UEI) calculations. An independent colour scale is applied to each city to preserve the spatial variability in PBLH within individual domains; consequently, colours should be interpreted within each panel rather than compared quantitatively between different cities.

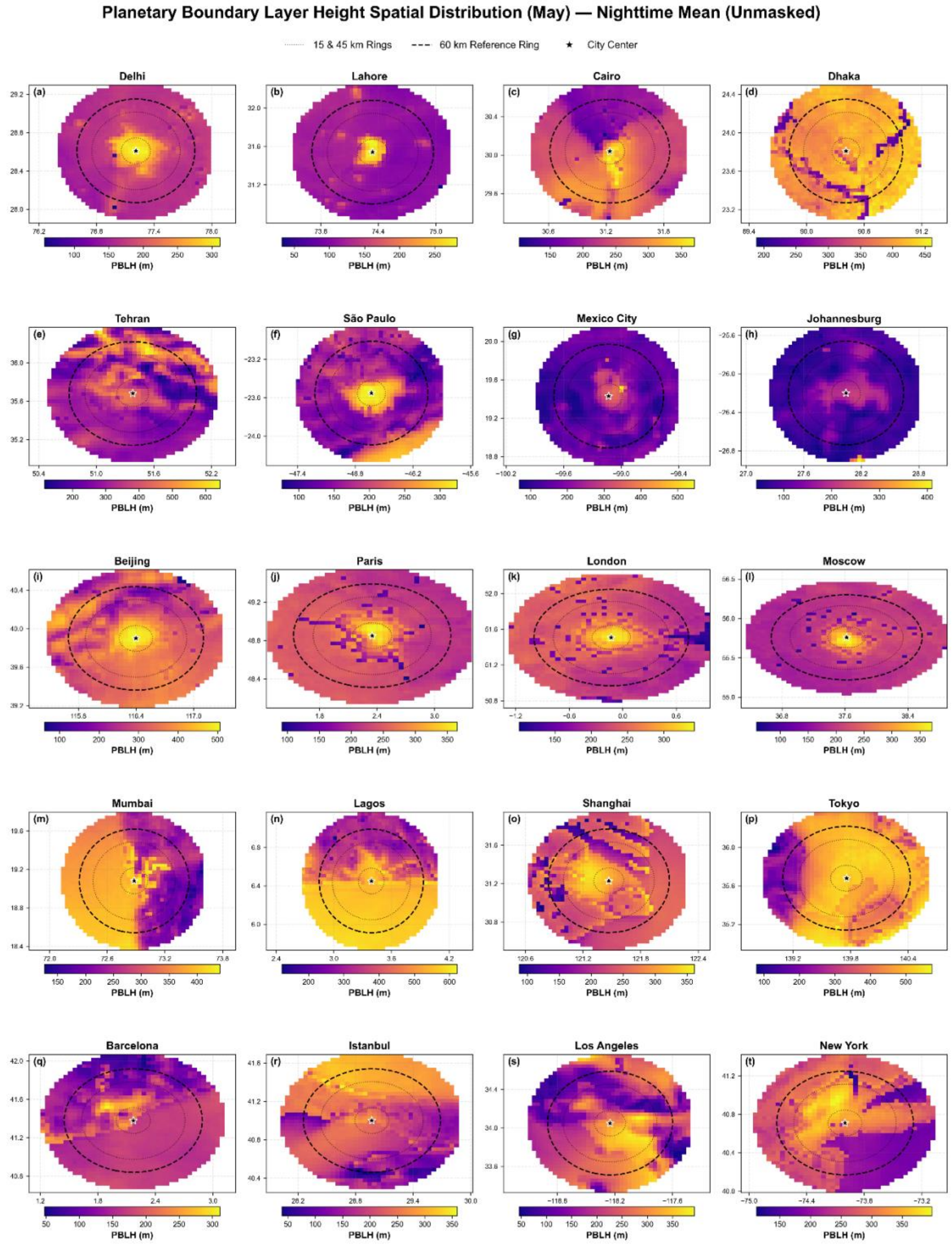

Figure S*23:* Spatial distribution of nighttime mean planetary boundary layer height (PBLH) for May 2024 obtained from the Simulated WRF simulations for the twenty study cities. Cities are grouped into non-coastal (top three rows) and coastal (bottom two rows) categories. The star marks the city centre, while the concentric circles indicate the 15 km urban-core boundary (dotted), the 45 km outer urban boundary (solid), and the 60 km reference radius (dashed) adopted for the radial analysis and Urban Effect Intensity (UEI) calculations. An independent colour scale is applied to each city to preserve the spatial variability in PBLH within individual domains; consequently, colours should be interpreted within each panel rather than compared quantitatively between different cities.

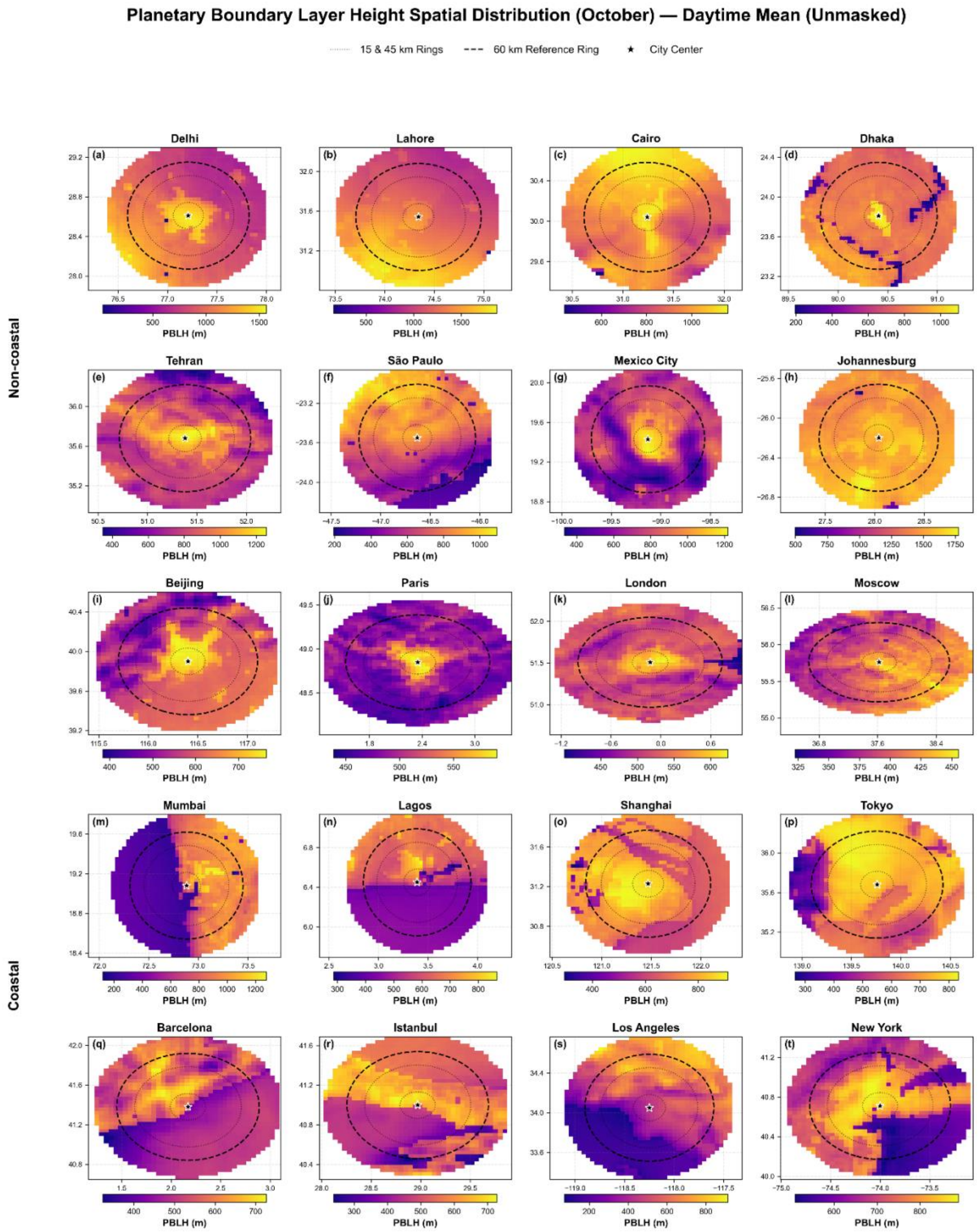

Figure S*24*: Spatial distribution of daytime mean planetary boundary layer height (PBLH) for October 2024 obtained from the Simulated WRF simulations for the twenty study cities. Cities are grouped into non-coastal (top three rows) and coastal (bottom two rows) categories. The star marks the city centre, while the concentric circles indicate the 15 km urban-core boundary (dotted), the 45 km outer urban boundary (solid), and the 60 km reference radius (dashed) adopted for the radial analysis and Urban Effect Intensity (UEI) calculations. An independent colour scale is applied to each city to preserve the spatial variability in PBLH within individual domains; consequently, colours should be interpreted within each panel rather than compared quantitatively between different cities.

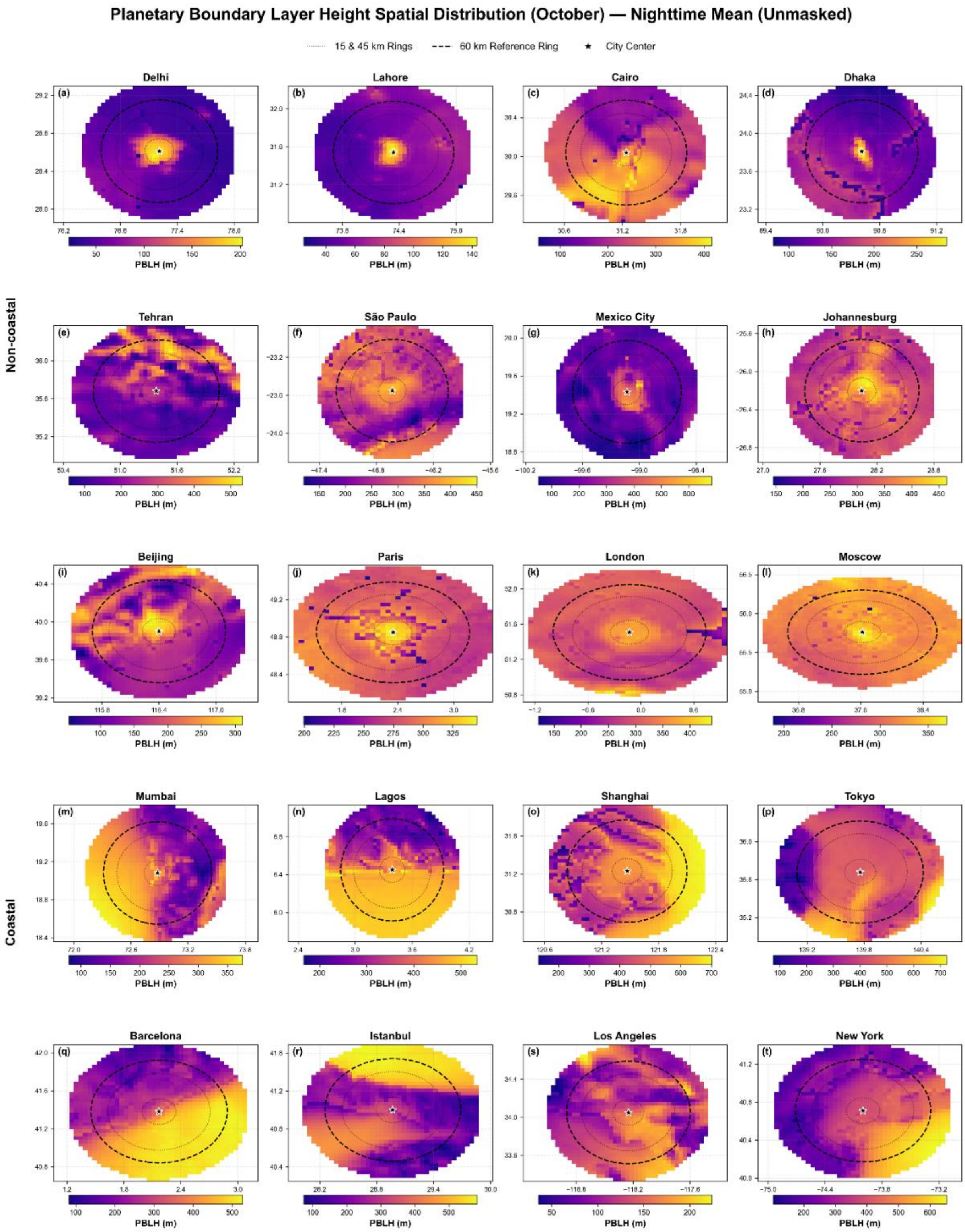

Figure S25: Spatial distribution of nighttime mean planetary boundary layer height (PBLH) for October 2024 obtained from the Simulated WRF simulations for the twenty study cities. Cities are grouped into non-coastal (top three rows) and coastal (bottom two rows) categories. The star marks the city centre, while the concentric circles indicate the 15 km urban-core boundary (dotted), the 45 km outer urban boundary (solid), and the 60 km reference radius (dashed) adopted for the radial analysis and Urban Effect Intensity (UEI) calculations. An independent colour scale is applied to each city to preserve the spatial variability in PBLH within individual domains; consequently, colours should be interpreted within each panel rather than compared quantitatively between different cities.

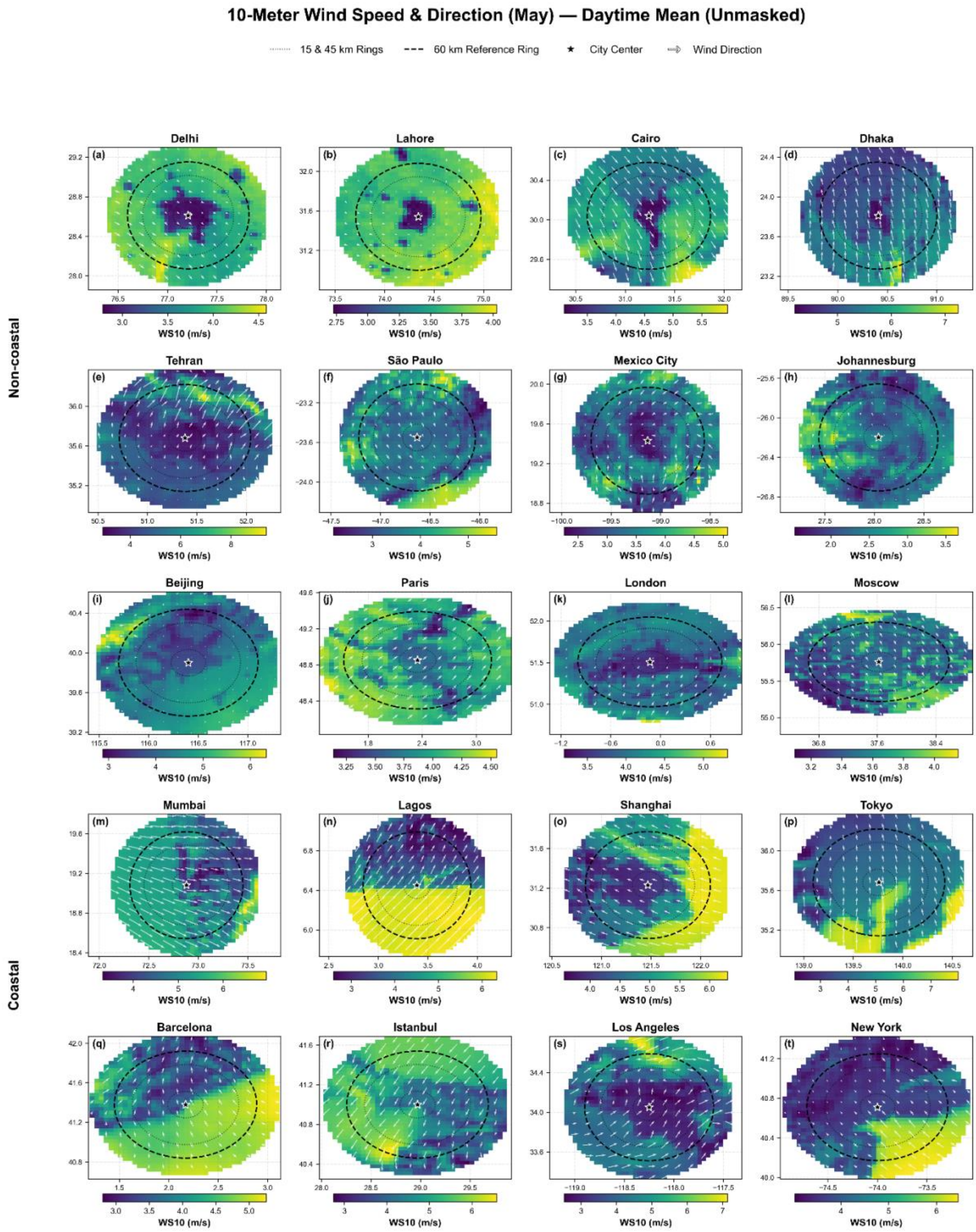

Figure S26: Spatial distribution of daytime mean 10 m wind speed (WS) and the corresponding mean wind vectors for May 2024 obtained from the Simulated (Prior to any adjustment) WRF simulations for the twenty study cities. Wind speed is shown by the colour shading, while white arrows indicate the mean near-surface wind direction and relative flow magnitude. Cities are grouped into non-coastal (top three rows) and coastal (bottom two rows) categories. The star marks the city centre, and the concentric circles indicate the 15 km urban-core boundary (dotted), the 45 km outer urban boundary (solid), and the 60 km reference radius (dashed) adopted for the radial analysis and Urban Effect Intensity (UEI) calculations. An independent wind-speed colour scale is used for each city to preserve the spatial variability within individual domains; therefore, colours should be interpreted within each panel rather than compared quantitatively between different cities.

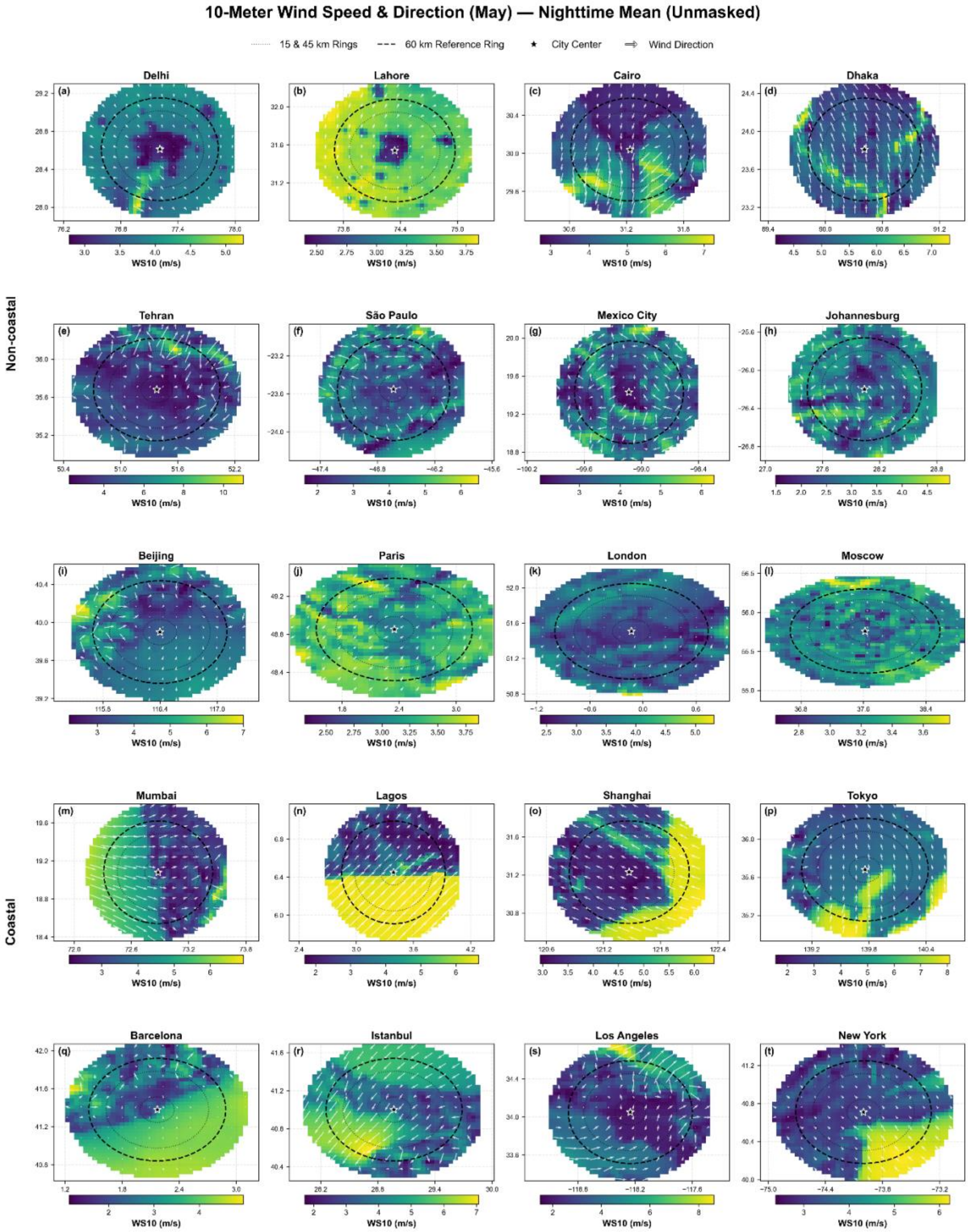

Figure S27**:** Spatial distribution of nighttime mean 10 m wind speed (WS) and the corresponding mean wind vectors for May 2024 obtained from the Simulated (Prior to any adjustment) WRF simulations for the twenty study cities. Wind speed is shown by the colour shading, while white arrows indicate the mean near-surface wind direction and relative flow magnitude. Cities are grouped into non-coastal (top three rows) and coastal (bottom two rows) categories. The star marks the city centre, and the concentric circles indicate the 15 km urban-core boundary (dotted), the 45 km outer urban boundary (solid), and the 60 km reference radius (dashed) adopted for the radial analysis and Urban Effect Intensity (UEI) calculations. An independent wind-speed colour scale is used for each city to preserve the spatial variability within individual domains; therefore, colours should be interpreted within each panel rather than compared quantitatively between different cities.

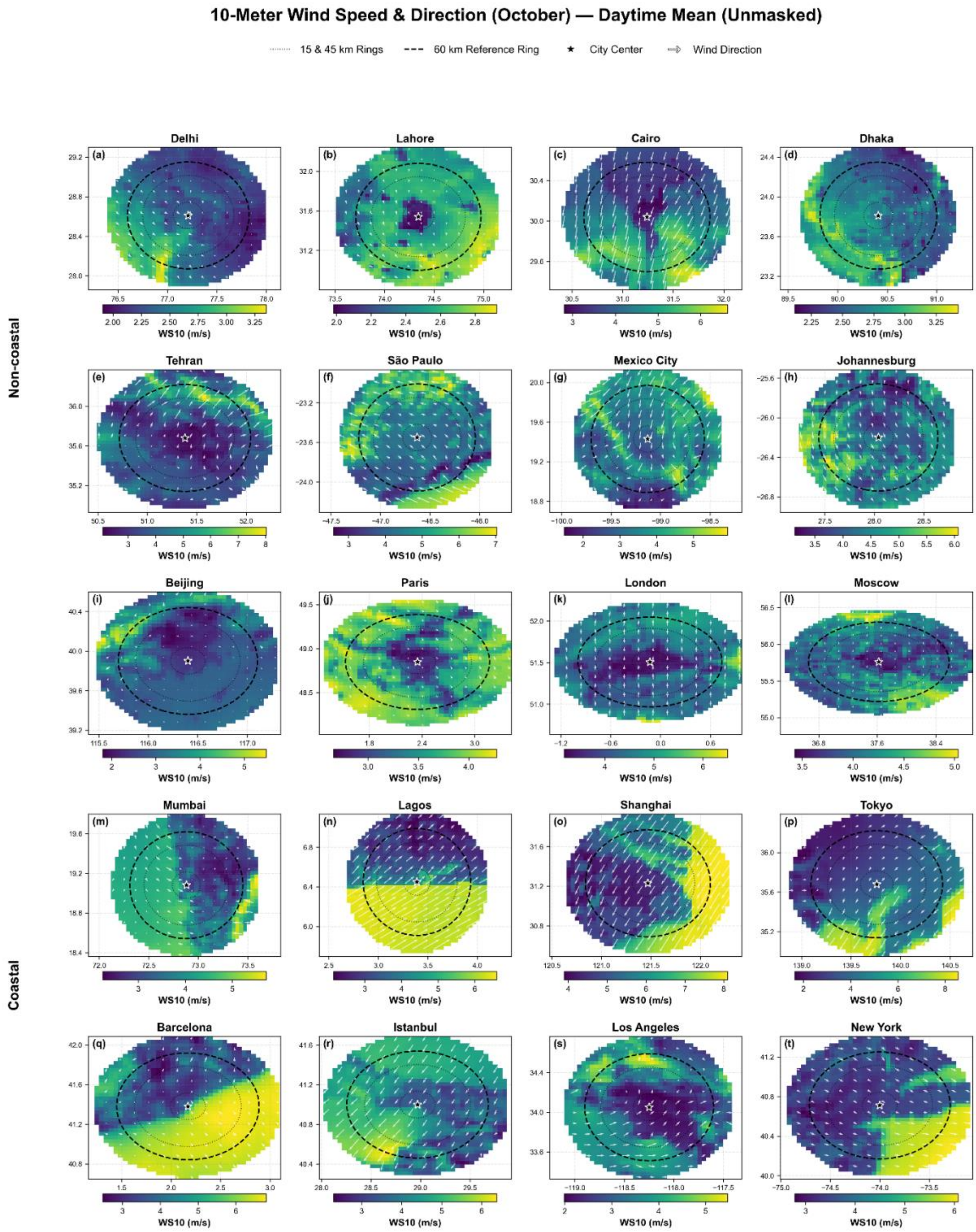

Figure S28: Spatial distribution of daytime mean 10 m wind speed (WS) and the corresponding mean wind vectors for October 2024 obtained from the Simulated (Prior to any adjustment) WRF simulations for the twenty study cities. Wind speed is shown by the colour shading, while white arrows indicate the mean near-surface wind direction and relative flow magnitude. Cities are grouped into non-coastal (top three rows) and coastal (bottom two rows) categories. The star marks the city centre, and the concentric circles indicate the 15 km urban-core boundary (dotted), the 45 km outer urban boundary (solid), and the 60 km reference radius (dashed) adopted for the radial analysis and Urban Effect Intensity (UEI) calculations. An independent wind-speed colour scale is used for each city to preserve the spatial variability within individual domains; therefore, colours should be interpreted within each panel rather than compared quantitatively between different cities.

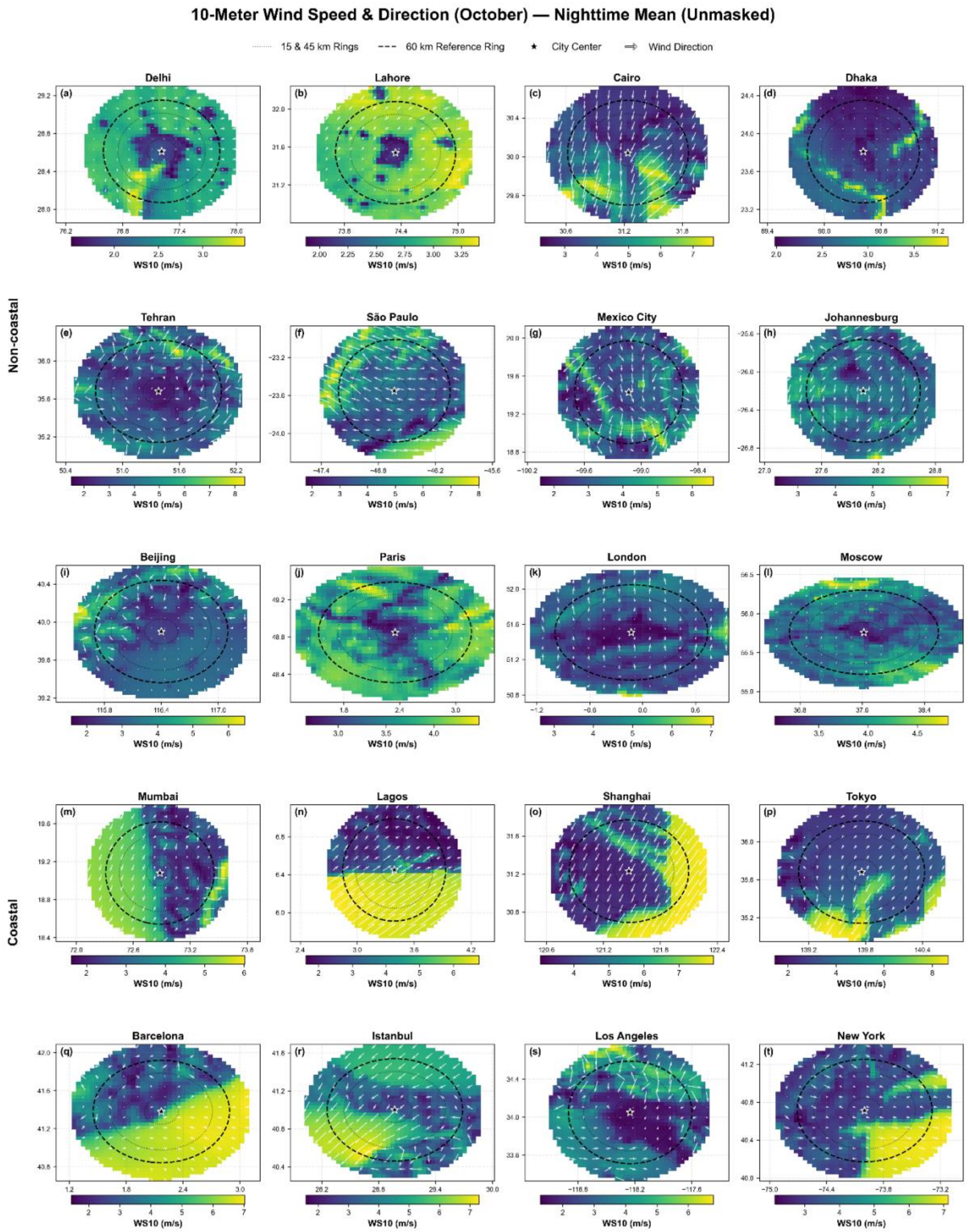

Figure S29: Spatial distribution of nighttime mean 10 m wind speed (WS) and the corresponding mean wind vectors for October 2024 obtained from the Simulated (Prior to any adjustment) WRF simulations for the twenty study cities. Wind speed is shown by the colour shading, while white arrows indicate the mean near-surface wind direction and relative flow magnitude. Cities are grouped into non-coastal (top three rows) and coastal (bottom two rows) categories. The star marks the city centre, and the concentric circles indicate the 15 km urban-core boundary (dotted), the 45 km outer urban boundary (solid), and the 60 km reference radius (dashed) adopted for the radial analysis and Urban Effect Intensity (UEI) calculations. An independent wind-speed colour scale is used for each city to preserve the spatial variability within individual domains; therefore, colours should be interpreted within each panel rather than compared quantitatively between different cities.